Bulletin of Volcanology (2019) 81:19
https://doi.org/10.1007/s00445-019-1281-1

RESEARCH ARTICLE

Linear inverse problem for inferring eruption source parameters from sparse ash deposit data as viewed from an atmospheric dispersion modeling perspective

Konstantin B. Moiseenko[1] · Nataliya A. Malik[2]

Received: 29 August 2018 / Accepted: 20 February 2019

Abstract
Determination of the volcanic eruption source parameters—total grain-size distribution and vertical ash mass distribution (VMD) within the source—is carried out on a collection of measured-area samples and granulometry data. For this, the geophysical inverse methods and Hybrid Particle and Concentration Transport Model (HYPACT) driven by wind and turbulence fields simulated with the Regional Atmospheric Modeling System (RAMS) are used. A two-step inversion procedure is proposed to obtain approximate but physically meaningful solution when the total number of ashfall samples is small and it is not possible to make a good initial guess of the source parameters. First, a spectrum of particle fall velocities is estimated by selecting a best-fit subset of aerodynamically distinct subpopulations of free and aggregate particles from the trial set used to simulate a polycomponent ashfall. The singular value decomposition (SVD) analysis is then employed to identify spatial components of the ash emissions' vertical distribution, as resolvable by the observations. Model validation experiments are conducted for the January 12, 2011, short-duration vulcanian explosion at Kizimen and paroxysmal phase of the December 24, 2006, sub-Plinian eruption at Bezymianny. The derived VMDs exhibit high variability in fine ash content (~ 60–100 wt%) as well as strong secondary maxima in the lower troposphere, likely reflecting the contribution of ash particles fallen out of co-pyroclastic flow ash clouds and partially collapsing eruption columns.

Keywords Volcanic ash · Aggregate fallout · Total grain-size distribution · Vertical ash mass distribution · Ill-posed problem · Regularization

Introduction

Over recent decades, numerical models of volcanic ash dispersal and fallout have become widely used to constrain eruption source parameters, such as total erupted mass (TEM), total grain-size distribution (TGSD), and a range of ash injection heights, from observations of tephra mass load and granulometry (see, for example, recent studies by Klawonn et al. 2012; Stuefer et al. 2013; Moxnes et al. 2014; Turner et al. 2014; Marti et al. 2017; White et al. 2017). Initial studies were based on simplified representation for transport and deposition (Suzuki 1983; Armienti et al. 1988; Carey and Sigurdsson 1982; Cornell et al. 1983), with Sparks et al. (1997) reviewing the state-of-the-art by the late 1990s. Comparing simulated mass loads against measurement data allows "best-fit" parameters to be selected using known inversion techniques: the downhill simplex method (Connor and Connor 2006); simple and weighted least squares (Pfeiffer et al. 2005; Costa et al. 2009; Bonasia et al. 2009; Spanu et al. 2016); and multiple least squares with some kind of regularization (Stohl et al. 2011; Klawonn et al. 2012; Moiseenko and Malik 2014). Provided that the meteorological fields are predicted correctly, the above model-based approach has important advantages over traditional sedimentological techniques (Pyle 1989; Bonadonna and Costa 2012) as it allows for intrinsic consistency between the measurement data, which are assumed to characterize the general features of the

Editorial responsibility: C. Bonadonna

✉ Konstantin B. Moiseenko
konst.dvina@gmail.com

[1] Atmospheric Composition Division, Obukhov Institute of Atmospheric Physics, Pyzhevskii per., 3, Moscow 119017, Russia

[2] Laboratory of Active Volcanism and Eruption Dynamics, Institute of Volcanology and Seismology Far East Branch RAS, Bulv. Piipa 9, Petropavlovsk-Kamchatsky 683006, Russia

Published online: 04 March 2019

particular deposit dispersal pattern, the derived estimates of the source parameters, atmospheric transport conditions, and particle settling velocities.

Since the complexity of the actual eruption source is often greater than the resolving power of the deposit data, the most important issue in selecting the source parameters is choosing the optimal (and, by necessity, highly limited) set of those model parameters that describe the most important aspects of the phenomena and can be determined uniquely from measurement data. This is commonly achieved by a parametric approach based on predefined simple functional forms for TGSD and vertical ash mass distribution (VMD) (Connor and Connor 2006; White et al. 2017). Additionally, an assumption about particle sphericity or constant shape factor is made to constrain ash particle settling rates (Bonasia et al. 2009; Klawonn et al. 2012). Although parametric methods are known to be highly efficient in geophysical investigations as well as atmospheric transport-related inverse problems, provided a suitable form for the prior distribution is chosen (Enting 2002; Debcedilski 2010), their application to an eruption source may be questionable on physical grounds, giving large variations in eruption styles and magnitudes for explosion events and phases of individual eruptions (Walker 1971, 1981; Sparks et al. 1997).

In this study, we consider the inverse problem for the eruption source parameters, where deposit data is sparse and observations on the eruption plume dynamics are very limited so that no good initial guess of TGSD and VMD can be made. The central problem of constraining the fall velocities of free and aggregate particles is solved by simulating numerically transport and sedimentation of particles comprising a trial set of model subpopulations. Selecting different optimal subsets of aerodynamically distinct subpopulations for each size bin of grain-size analyses then provides an implicit account for the commonly observed variation in component abundances (morphology) with particle size (Walker 1971; Wohletz et al. 1989), which may be important in constraining particle settling velocities from polycomponent ashfalls. This approach has been shown to allow for significant reduction in the total number of unknowns of the problem, resulting in model-predicted deposit dispersal patterns that are generally consistent with field data (Moiseenko and Malik 2014). The original non-parametric procedure of Moiseenko and Malik (2014) is extended to invert TEM, TGSD, and VMD of bulk ash as well as fine and coarse ash fractions. The inversion procedure uses well-developed regularization techniques (subset selection, truncated singular value decomposition) to obtain an approximate, but physically meaningful solution constrained by ashfall deposit data and independent observations of the heights of the eruption column and the downwind ash plume.

The model validation experiments were conducted for the January 12, 2011, VEI = 2 short-duration vulcanian explosion at Kizimen Volcano and the December 24, 2006, VEI = 2–3 sub-Plinian eruption of Bezymianny (termed the KZ11 and BZ06 ashfalls here). Ash simulations were performed using the Hybrid Particle and Concentration Transport Model (HYPACT) driven by wind and turbulence fields simulated with the Regional Atmospheric Modeling System (RAMS) (www.atmet.com). Although eruptions with a higher explosivity index are obviously of greatest interest concerning their environmental and geological impacts, we feel that the present study provides insights into those aspects of the inversion problem which are relevant to a substantially wider range of eruption magnitudes and dispersive powers, including a broad spectrum of particle fall velocities, large and poorly controlled uncertainties in simulating dispersion of ash particles by mesoscale turbulence, and a low signal-to-noise ratio in the measurement data.

Theoretical considerations

Basic assumptions

We consider a population of particles, R_{mod}, emitted from an eruption source occupying a volume Ω in the computation domain and representing a highly simplified approximation to a natural source of volcanic ash formed by all the processes relevant to turbulent convective mass transfer, inter-phase changes, and secondary fragmentation within an eruption column as well as elutriation of fine ash from pyroclastic flows (PF). We call this a "convective stage" of atmospheric transport as opposed to a simulation of a "downwind plume" stage in which ash particles are transported by atmospheric wind. It is then assumed that R_{mod} represents the sum of contributions from the vent-originated eruption plume and co-PF clouds, with each particle from R_{mod} settling at either its individual terminal fall velocity or a collective settling speed of the respective aggregate particles. We further refer to the above ash particle classes, differentiated with respect to settling conditions, as free (F) and aggregate (A) classes, so that $R_{\mathrm{mod}} = \mathrm{F} \cup \mathrm{A}$ (see Appendix 1 for basic notations).

The simplest geometric model of the eruption source, sufficient for the purposes of this study, is a vent-centered cylinder of radius R_s, representing a characteristic horizontal scale of the eruption dynamic-driven stage of atmospheric transport, and length $z_c = z_t - z_b$, where z_b is the vent altitude according to the model topography and z_t is the top height of the eruption column. Apart from the prescribed spatial geometry, the source is characterized by a time-independent emission rate $q(z)/\Delta t$ [kg m^{-1} s^{-1}], where Δt is the emission time duration, such that $q(z)\,\partial z$ gives a total mass of particles emitted within a range of heights from z to $z + \partial z$. The other commonly used assumptions are as follows: (i) formation of ash aggregates in the downwind plume stage can be neglected and (ii) all particles within the source are uniformly mixed irrespective of their

terminal fall velocities; consequently, for any subpopulation of particles discriminated by particle size and morphology, the corresponding VMD is proportional to the VMD of R_{mod}.

Validity of the above assumptions should be checked a posteriori as part of the inversion procedure. Although formation and growth of ash aggregates and mixed ash/water and ash/ice hydrometeors may take place within a dispersed ash plume through a variety of processes (Textor et al. 2006; James et al. 2002, 2003; Mangan et al. 2017; Durant et al. 2008; Steinke et al. 2011), violation of assumption (i) concerning the non-interacting particle classes does not seem to have a strong effect on the results of the present computations. This is because the characteristic times of ash fallout are relatively short (≤ 1 h), thus simulations of sedimentation can be performed using time-independent settling speeds. Assumption (ii) concerning uniform mixing assumes no gravitational separation of ash-sized particles, which may be a reasonable first-guess approximation for the true VMD (Moiseenko and Malik 2014) in the absence of direct observations of grain-size variations with altitude in an eruption column. Using 63 μm as an approximate upper limit for the size of elutriated ash particles (Girina (1991), Bezymianny volcano; see also Evans et al. (2009)), one may consider a total VMD as the sum of inputs from a coarse ash (> 63 μm) fraction, with the eruption plume as its primary origin, and a fine ash (≤ 63 μm) fraction whose VMD combines the effects of the eruption plume and co-PF clouds, so that $q(z) = q_c(z) + q_f(z)$, where the lower indexes c and f are used henceforth to denote quantities related to the coarse and fine ash fractions, respectively. Apart from physically motivated discrimination between the primary emission sources (i.e., eruption plume and co-PF clouds; for more discussion, see Cornell et al. 1983; Rose and Durant 2009; Evans et al. 2009; Bonadonna et al. 2002), the above approach allows the effects of size-induced gravitational sorting of ash particles in the convective stage to be estimated. We then apply the model of spatially uniform source either to the total ash fraction of pyroclasts (*bulk ash-based approach*) or to each of the above defined size fractions (*fraction-based approach*), with specific examples given in section "Inversion results."

The model of Wilson and Huang (1979) (referred to as WH henceforth) is employed to describe the combined effect of shape and roughness on falling speed of free particles by using a single shape parameter F (shape factor) (Riley et al. 2003; Liu et al. 2015). It is assumed that particle aggregates fall at speeds of equivalent solid spheres ($F \equiv 1$), with "equivalent aggregate diameter" d_a (following the terminology of James et al. 2002) and density ρ_a treated as adjustable parameters in the model (Mastin et al. 2016). Consequently,

$$v_t = v_{\mathrm{WH}}(\rho, F, d)\ (\text{free particles}) \tag{1a}$$

$$v_t = v_{\mathrm{WH}}(\rho_a, 1, d_a)\ (\text{ash aggregates}) \tag{1b}$$

where v_t is the settling speed of ash particle of size d and density ρ from F and A classes, respectively, and v_{WH} is the fall velocity of the WH model.

In the present simulations, R_{mod} is divided among L equal-sized (on a phi scale) bins, k (=k_1, ... k_L), of the grain-size analyses of ash deposit samples so that ash particles in bin k have sizes from 2^{-k} to 2^{-k+1} mm (the lower subscript k will be used to denote a quantity related to bin k). For each k, we define a trial set $\{S_{k,p}\}_{p=1}^{P+Q}$ of model subpopulations such that

$$R_{\mathrm{mod}} = \cup_{k=k_1}^{k_L} (R_{\mathrm{mod}})_k, (R_{\mathrm{mod}})_k = \cup_{p=1}^{P+Q} S_{k,p}, \tag{2}$$

where the first P subpopulations ($S_{k,\,1}$ … $S_{k,\,P}$) and the remaining Q subpopulations ($S_{k,\,P+1}$ … $S_{k,\,P+Q}$) consist of F- and A-particles, correspondingly, with each subpopulation characterized by the joint distribution of eitherρ, F and d (F-particles) or ρ_a, d_a (A-particles).

Let R be an *initial population*, following terminology of Walker (1971), representing the total assemblage of ash-sized pyroclasts composing a particular ashfall deposit. The key assumption of the inversion consistent with Eqs. (2) is that for each k (bin size), there exists an optimal, in a statistical sense, subset from the above trial set, composed of a highly limited number of model subpopulations $S_{k,\,p}$, which approximates sufficiently accurately the true unknown distribution of k-particles in R with respect to their settling velocities.

In the above formulation, the words "a highly limited number" are important in order for the results of inversion based on a limited amount of field data be statistically significant. Any given choice for model particle subpopulations is highly subjective, since it is always a compromise between the model complexity, when trying to account for a broad range of particle settling velocities, and the amount of available measurements. An approach for constraining the trial set of model subpopulations adapted to the present simulations is discussed in section "Forward simulations."

The inverse problem

Let $\mathbf{y} = \{y(\mathbf{r}_i)\}_{i=1}^{I}$ be an observation vector representing mass loads (mass per area values, kg m^{-2}) measured at sample sites $\mathbf{r}_1, \ldots, \mathbf{r}_I$. The grain-size analysis of the first $I_g \le I$ measured-area samples will also yield L data vectors $\mathbf{y}_k \equiv \{y_k(\mathbf{r}_i)\}_{i=1}^{I_g}$, $k = k_1, \ldots k_L$. (The bold symbols are used conventionally to denote vector quantities.) A discrete representation for the inverse problem is obtained by dividing the volume Ω into J model sources: $\Omega = \cup_{j=1}^{J} \Omega_j$, where Ω_j represents a disk of radius R_s and height $\Delta z_j = z_{j+1} - z_j$, $j = 1, \ldots J$ ($z_1 \equiv z_b$, $z_{J+1} \equiv z_t$). Assume for definiteness that $J < I$, so that the problem of VMD retrieval (Eq. (10) below) is overdetermined with respect to the total number of unknowns (Jackson 1972).

The theoretical (model-predicted) mass load $\hat{y}_k$ at a location $\mathbf{r}$ on the ground is given according to Eq. (2) by

$$\hat{y}_k(\mathbf{r}) = \sum_{j=1}^{J}\sum_{p=1}^{P+Q}\gamma_{k,p,j}\cdot g_{k,p,j}\left(\mathbf{r};\mathbf{u},\mathbf{u}',v_t,R_s,\Delta z_j\right), \quad (3)$$

where $\gamma_{k,\,p,\,j}$ is the total mass of $S_{k,\,p}$-particles emitted from a jth model source (Ω_j), and $g_{k,\,p,\,j}(\mathbf{r})$ is the probability that a particle emitted from Ω_j will settle at $\mathbf{r}$ which is preconditioned on the resolved wind ($\mathbf{u}$), atmospheric turbulence ($\mathbf{u}'$), settling velocity (v_t), and source dimensions (R_s, Δz_j) and must be computed from the atmospheric transport model. Using the assumption of uniform mixing of particles within the source, we can write

$$\gamma_{k,p,j} = M_j\cdot\xi_{k,p}, \quad (4)$$

so that

$$\hat{y}_k(\mathbf{r}) = \sum_{j=1}^{J} M_j\sum_{p=1}^{P+Q}\xi_{k,p}\cdot g_{k,p,j}(\mathbf{r}), \quad (5)$$

where $\xi_{k,\,p}\geq 0$ is a weight fraction of $S_{k,\,p}$-particles in the TEM, $\Sigma_{k=k_1}^{k_L}\Sigma_{p=1}^{P+Q}\xi_{k,p}=1$, and $M_j\left(=\int_{z_j}^{z_{j+1}}q(z)\,dz\right)$ is the total mass of ash particles emitted from the jth model source.

Using the bulk ash-based approach (see sub-section "Basic assumptions"), the complete observational model relating the measured data to model predictions is given by vector equations

$$\mathbf{y}_k = \hat{\mathbf{y}}_k + \boldsymbol{\varepsilon}_k, k = k_1,\ldots k_L, \quad (6)$$

$$\mathbf{y} = \hat{\mathbf{y}}_{k_1} + \ldots + \hat{\mathbf{y}}_{k_L} + \boldsymbol{\varepsilon}, \quad (7)$$

where $\boldsymbol{\varepsilon}_k$ and $\boldsymbol{\varepsilon}$ are unknown random ($I_g\times 1$) and ($I\times 1$) vectors representing the total discrepancy between the model-predicted and observed mass loads (we will refer to particular elements in $\boldsymbol{\varepsilon}_k$ and $\boldsymbol{\varepsilon}$ as model prediction errors). The inverse problem associated with Eqs. (5, 6, and 7) consists of determining for each k the best-fit subset of subpopulations $S_{k,p}$, $S_k^*\subseteq(1,2,\ldots,P+Q)$, along with the corresponding coefficients $\xi_{k,\,p}$ and M_j given the measurement vectors $\mathbf{y}$ and $\mathbf{y}_k$, $k=k_1,\ldots k_L$.

An approximate solution to systems (6, 7) is obtained by successive approximations starting with a vertically homogeneous source with a height-independent emission rate ($q=$ const) constrained by independent estimates for z_b and z_t.

Step I. Setting $M_1=M_2=\ldots=M_N=\tilde{M}$, $x_{k,p}=\tilde{M}\cdot\xi_{k,p}$, we solve for $\mathbf{x}_k=(x_{k,\,p=1},x_{k,\,p=1}\ldots x_{k,\,p=P+Q})$ so that

$$\mathbf{y}_k' = \mathbf{A}_k'\mathbf{x}_k, \quad k=k_1,\ldots k_L, \quad (8)$$

where $\mathbf{y}_k' = \mathbf{W}_k\mathbf{y}_k$, $\mathbf{A}_k' = \mathbf{W}_k\mathbf{A}_k$, $\mathbf{A}_k$ is $I_g\times(P+Q)$ matrix with elements $a_{i,p}=\sum_{j=1}^{J}g_{k,p,j}(\mathbf{r}_i)$, with pth column of the matrix representing input from the subpopulation $S_{k,\,p}$, and $\mathbf{W}_k$ is an ($I_g\times I_g$) prediction error covariance matrix (see sub-section "Simulation scenarios"). Let $\hat{\mathbf{x}}_k$ be a solution to Eq. (8) so that a first-guess approximation to $\xi_{k,\,p}$ is given by

$$\hat{\xi}_{k,p} = \hat{x}_{k,p}/\tilde{M}, \qquad \tilde{M}=\sum_{k=k_1}^{k_L}\sum_{p=1}^{P+Q}\hat{x}_{k,p}, \quad (9)$$

where $\tilde{M}\cdot J$ gives the first-guess approximation to TEM of ash particles in all size bins.

Step II. Invoking $\hat{\xi}_{k,p}$ into Eq. (5) and summing over k according to Eq. (7), we seek a solution $\hat{\mathbf{m}}$ to the system

$$\mathbf{y}' = \mathbf{B}'\mathbf{m}, \quad (10)$$

where $\mathbf{y}'=\mathbf{W}\mathbf{y}$, $\mathbf{B}'=\mathbf{B}\,\mathbf{m}$, $\mathbf{m}=(M_1,\ldots M_J)$ is a ($J\times 1$) vector of unknowns, $\mathbf{W}$ is an ($I\times I$) model error covariance matrix, and $\mathbf{B}$ is a ($I\times J$) matrix with elements

$$(b_0)_{i,j} = \sum_{k=k_1}^{k_L}\sum_{p=1}^{P+Q}\hat{\xi}_{k,p}\cdot g_{k,p,j}(\mathbf{r}_i). \quad (11)$$

One can finally obtain the following estimates:

$$M_{\text{tot}} = \sum_{j=1}^{J}\hat{M}_j, \quad (12)$$

$$\Delta M_k = M_{\text{tot}}\sum_{p=1}^{P+Q}\hat{\xi}_{k,p}, \quad k=k_1,\ldots k_L, \quad (13)$$

where M_{tot} is the TEM of ash particles, and $(\Delta M_{k_1},\Delta M_{k_2},\ldots,\Delta M_{k_L})$ and $\left(\hat{M}_1,\hat{M}_2,\ldots,\hat{M}_J\right)$ represent the discrete approximations for TGSD and VMD, respectively. The important advantage of using Eq. (7) in the second step of the inversion procedure is that, in the absence of significant bias in measured mass loads and model simulations, the prediction errors of the size bin-related problems in Eq. (8) are expected to partially compensate each other by summing k, which results in more stable estimates for VMD. Additionally, the bulk ash-based approach provides the best strategy in the case of small grain-size samples (i.e., when $I_g<<I$), as the whole set of measurement data is used for the simulations. Alternatively, one may use the fraction-based approach (see sub-section "Basic assumptions") and consider vector equation which is similar to Eq. (7) but related to mass loads for either the coarse or fine ash faction, with the only difference being that the summing of k in Eqs. (7, 9, and 11) is performed over a subset of k indexes related to the size fraction. The system (10) is then solved separately for each fraction to obtain the total VMD and TEM of ash, given by $\hat{M}_j=\left(\hat{M}_j\right)_c+\left(\hat{M}_j\right)_f$ and $M_{\text{tot}}=(M_{\text{tot}})_c+(M_{\text{tot}})_f$, along with a mass fraction of the fine ash particles $(m_{63})_j=\left(\hat{M}_j\right)_f/\hat{M}_j$, $m_{63}=(M_{\text{tot}})_f/M_{\text{tot}}$. The complete description of the inversion technique is provided in Appendix 2.

Volcanological setting

Below, we consider two well-studied eruptions from currently active volcanoes at Kamchatka Peninsular—the complex

andesitic stratovolcanoes of Bezymianny and Kizimen (Fig. 1)—to assess the general validity of the proposed inversion approach under different atmospheric transport conditions and eruption styles.

The January 12, 2011, ashfall from Kizimen

Kizimen volcano (55° 08.0′ N, 160° 19.3′ E, altitude 2376 m) is located in the central part of the eastern volcanic belt of Kamchatka (Melekestsev et al. 1995). The newest cycle of explosive-extrusive-effusive activity at Kizimen began in October 2010 (Malik and Ovsyannikov 2011). Since then, increased seismic activity at the volcano has been recorded continuously along with ash plumes of varying thicknesses traveling as far as 500 km downwind at tropospheric to sub-statospheric levels. Here, we study the January 12, 2011, explosive event, with the eruption start time (20:38 UTC, January 13 07:38 local time) and duration (10 min) constrained by seismic data from the Kamchatka Branch of the Russian Academy of Sciences Geophysical Service (http://www.emsd.ru/~ssl/monitoring/main.htm). Strong (30–50 ms^{-1}) unidirectional winds in a free troposphere resulted in the ash plume moving rapidly downwind at a visually estimated altitude of 5–6 km (N.A. Malik, ground observations 60 km from the vent; all heights from here on are above sea level). The fan-like deposit dispersal pattern (Fig. 1) had a small angle of spread and was probably produced by the simultaneous deposition of ash particles from the eruption column and co-PF clouds, as supported by the results of present simulations (see below). The total mass of the KZ11 fall deposit was estimated using a single straight-line approximation on the log mass–$area^{1/2}$ plot (Fierstein and Nathenson (1992), Eq. (12) with thickness T converted to mass load) to be equal to 0.6–1.2 × 10^9 kg. Grain-size distribution (GSD) analysis was performed on 12 measured-area samples (Table 1) using a combination of sieve and laser diffraction analyses to

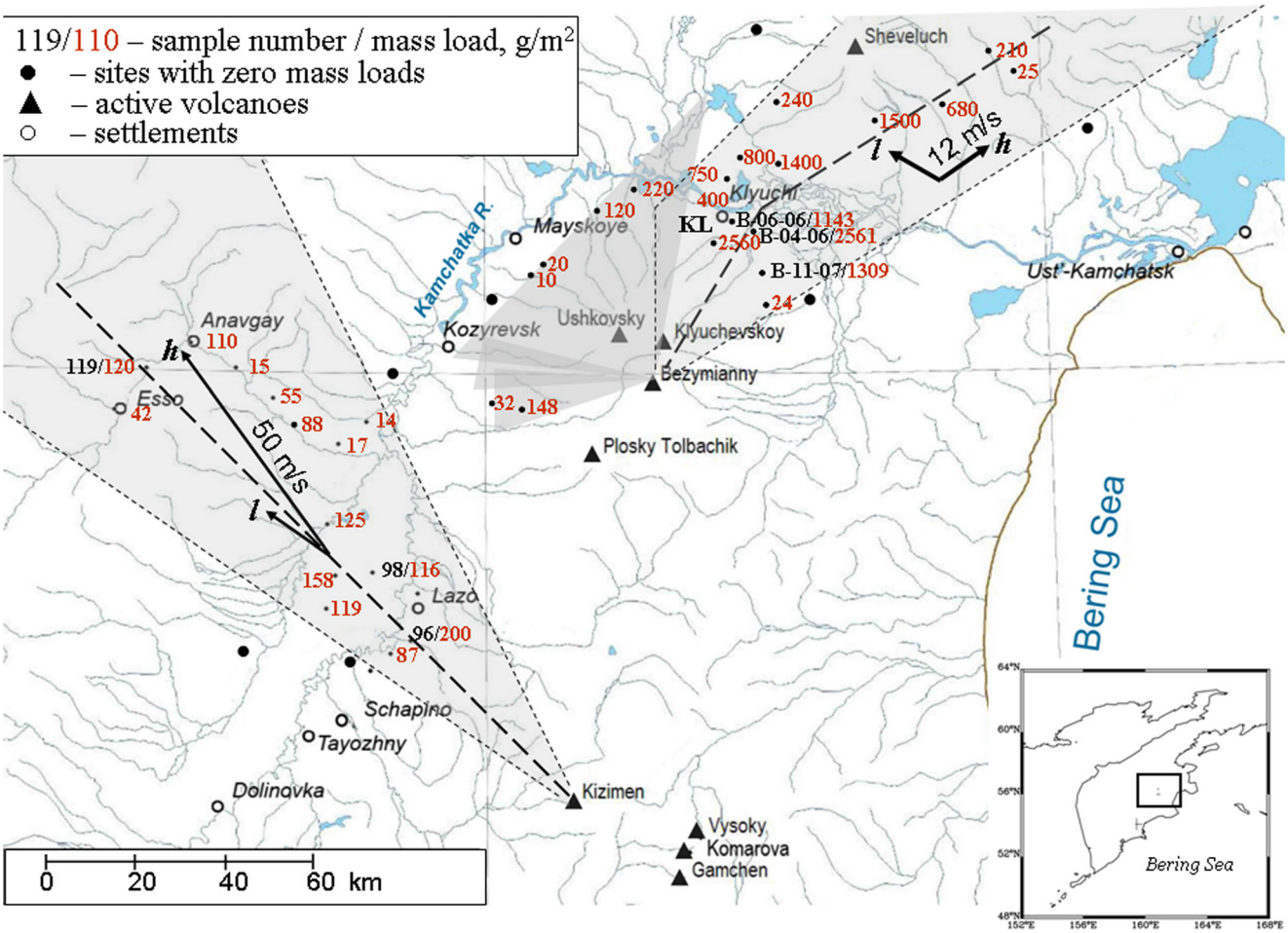

Fig. 1 The BZ06 Plinian fall and the KZ11 ashfall deposits (light gray; dashed line marks deposit dispersal axis) and the BZ06 ashfall from co-PF clouds and a lower part of the eruption column (dark shaded area WSW–N from Bezymianny). Black arrows, whose length is scaled with the wind speed, show wind speeds and directions at heights of the ash plumes (h) and 850 mbar (~ 1.5 km a.s.l.) (l) at the time of ashfalls basing on atmospheric soundings at Klyuchi radiosonde station (KL, ~ 40 km N from Bezymianny) (http://weather.uwyo.edu/upperair/sounding.html)

obtain GSDs from the KZ11 fall deposit within the 0.5–1000 μm size range (size bins from $k = 1$ to $k = 11$).

The December 24, 2006, ashfall from Bezymianny

Bezymianny Volcano (55° 58.7′ N, 160° 35.2′ E, altitude 2880 m) is located in the central part of the Klyuchevskaya volcanic group about 10 km SSW of Klyuchevskoy volcano. The current activity started with a catastrophic eruption in 1956 (Girina 2013). Short explosive eruptions, occurring once or twice a year, are accompanied by pyroclastic flows and effusion of viscous lava, with ash plumes rising up to 6–15 km (all heights are given above sea level). The culminating phase of the December 24, 2006, eruption (start time 09:17 UTC, 21:17 local time) lasted ~ 50 min and was accompanied by strong pyroclastic flows (volume 0.006–0.008 km^3, runout distance of ~ 6.5 km) (Girina 2013), a steady eruption column reaching 13–15 km (night-time observations of lightning), a laterally spreading umbrella cloud (satellite imagery), ash fallout (visually observed as ash/snow mixture 40 km from the vent), and downwind ash plume at an altitude of ~ 10 km traced as far as 850 km NE of the volcano (Malik 2011).

Compared to the KZ11 event, a wider range of injection heights and strongly veering winds below 300 mbar at the time of the BZ06 ashfall resulted in partially overlapping deposits produced by ash which fell out of either the umbrella cloud or the lower part of the eruption column and co-PF clouds (Fig. 1), with the model-predicted ranges of injection heights of 8–15 km and 2–8 km, respectively (see section "Inversion results"). We refer to these areas of the deposit as the Plinian and co-PF parts of the BZ06 deposit, respectively.

The TEM of the tephra fall deposit was earlier estimated to be $4.0–6.7 \times 10^9$ kg, using the PlumeRise model (Woodhouse et al. 2013) and $\geq 3.8 \times 10^9$ kg (based on izomass map) (see Moiseenko and Malik (2014) for details). Sixteen samples from the BZ06 Plinian fall deposit were sieved at 1Φ intervals down to 63 μm to measure the GSD within the range 63–500 μm as well as the fine ash fraction (m_{63}) (Table 1). Additionally, three of the above 16 samples collected at distances 30–40 km from the vent were analyzed using a combination of sieve and laser diffraction analyses to obtain GSDs of the BZ06 Plinian fall deposit in the 0.5–500 μm size range (size bins 2–11). According to Fig. 2, the GSDs of the KZ11 and BZ06 fall deposits are polymodal and have a low degree of sorting at all distances from the vent, which can be explained by ash aggregation, a wide range of particle fall velocities, and a combination of the co-PF and eruption plume fallouts. Significant contributions of all these factors are shown clearly in the results of our simulations.

Forward simulations

RAMS/HYPACT modeling system

Numerical simulations of atmospheric ash dispersal and fallout were performed with the Hybrid Particle and Concentration Transport model (HYPACT) (Tremback et al. 1994; Walko and Tremback 1995) driven by three-dimensional (3D) wind, potential temperature, and turbulent kinetic energy fields simulated by the Regional Atmospheric Modeling System (RAMS) limited area weather forecast model (Pielke et al. 1992; see also: www.atmet.com). The initial and boundary conditions for the RAMS simulations were determined using the National Center for Environmental Prediction's Final Operational Global Analysis (NCEP FNL) meteorological dataset on a 6-h basis.

Numerical computations of meteorological fields and ash dispersal were performed using three nested polar stereographic grids G1–G3 (Fig. 3). The outer G1 and first inner grid, G2, have horizontal dimensions of 40×40 and 70×70 and horizontal resolutions of $\Delta_x = 60$ and $\Delta_x = 15$ km, respectively. The G1 and G2 grids are common in our ash dispersal simulations for active volcanoes in the Kamchatka-Kuril arc and allow large scale weather systems traveling across the region to be resolved. The second inner grid, G3 (107×107, $\Delta_x = 3$ km), is centered on the volcano location and enables topography-generated atmospheric motions on scales ≥ O (10 km) to be resolved. The three grids have similar vertical structures, with spacing between adjusting layers varying from 200 m near the surface to ~ 700 m in the upper troposphere and lower

Table 1 Ashfall sample data

Ashfall deposit	I (I_g)	ΔL (ΔL_g), km	Δd, μm	m_{63}	ΔM, g m^{-2}
BZ06	40 (16)	23–105 (31–93)	0.5–500	0.53–.84	10–2560
KZ11	12 (12)	51–136 (51–136)	0.5–1000	0.59–.85	42–200

I total number of ash deposit samples, I_g number of grain-size samples, ΔL the sampling distance range from the source volcano, ΔL_g, those for the grain-size samples, Δd particle size range (LDA and sieve analyses), m_{63} mass fraction of fine ash particles (≤ 63 μm), ΔM total range of the mass loads

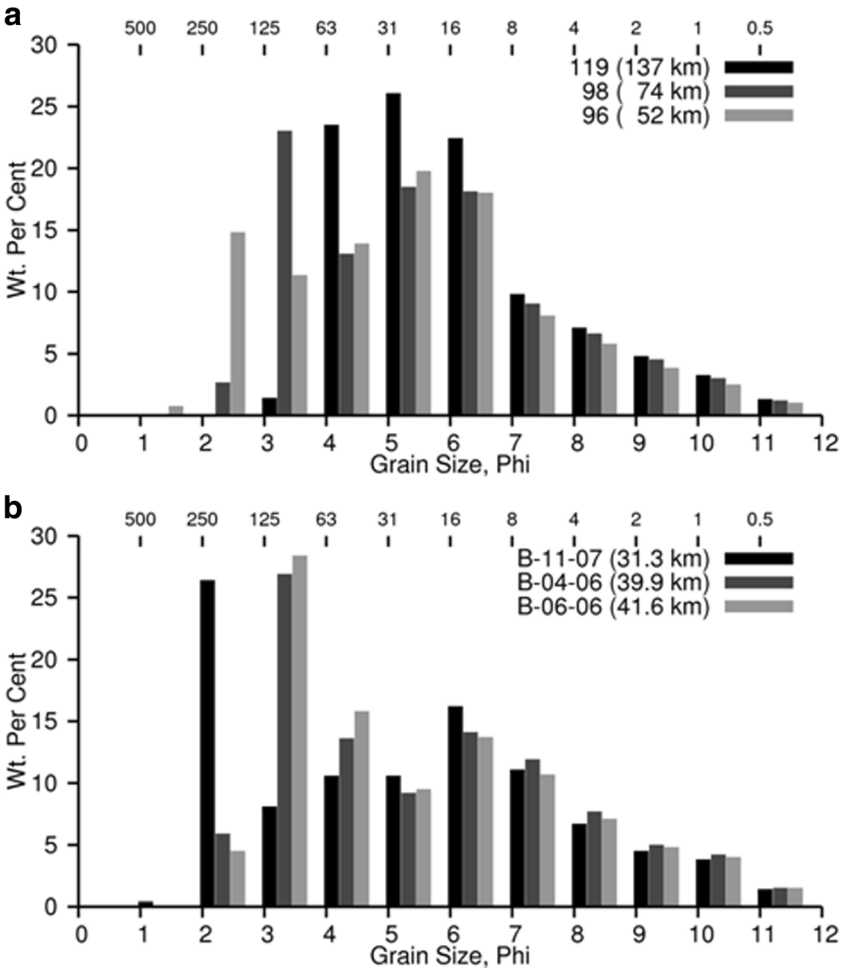

Fig. 2 Grain-size distributions of intermediate fallout from the KZ11 (**a**) and BZ06 (**b**) eruptions. A key is "sample number/ distance from vent"

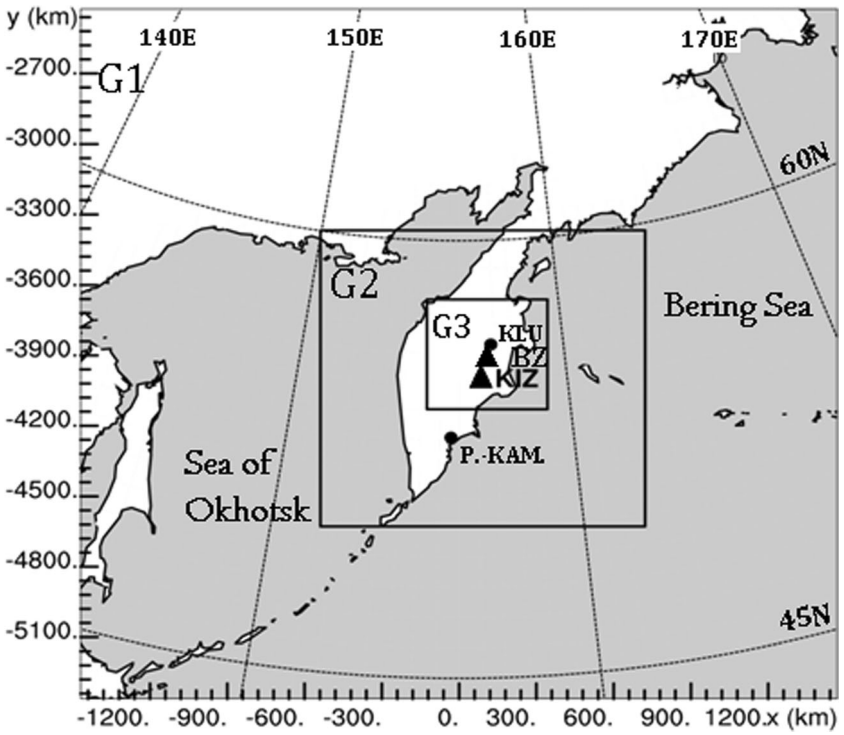

Fig. 3 Domains of 60 × 60 km (G1), 15 × 15 km (G2), and 3 × 3 km (G3) nested grids used for the simulations of ash transport and deposition. KIZ, Kizimen Volcano; BEZ, Bezymianny Volcano; KLU, Klyuchi radiosonde launch site; P.-KAM, Petropavlovk-Kamchatskii Town. Horizontal coordinates *x* and *y* of the computational grid are coordinates in a polar stereographic projection

stratosphere (40 vertical layers). The RAMS model output was saved as 30 min averages of corresponding instantaneous three-dimensional meteorological fields.

We use a Lagrangian (random-flight) model HYPACT driven by RAMS-calculated meteorological fields to simulate atmospheric transport in a randomly fluctuating wind field by tracing large amounts of model particles carrying a prescribed mass of ash attributed to a given subpopulation ($S_{k,\ p}$) and emission source (Ω_j). The random-flight models are known to be the most appropriate tool to simulate three-dimensional atmospheric dispersion in inhomogeneous turbulence (Wilson and Sawford 1996; de Haan and Rotach 1998; Yamada and Bunker 1988; Turner et al. 2014). The original Fortran 90 code of HYPACT model has been upgraded to simulate fallout of ash-sized pyroclasts incorporating the assumption that motion of individual ash particles or aggregates responds to all frequencies of atmospheric turbulent motions (i.e., effect of particle inertia is negligibly small), which seems to be a reasonable assumption for particles less than 1–2 mm (Wang and Stock 1993).

Ash transport simulations

Volcanic source geometry In the BZ06 simulations, the source radius R_s is set to 12 km which is the maximum crosswind diameter of the umbrella cloud according to satellite images (Moiseenko and Malik 2014). Assuming a proportionality between R_s and z_c (Golitsyn et al. 1989), the above estimate is reduced to $R_s = 8$ km as a representative value for the KZ11 eruption cloud. Variation of the above estimates within a factor of 1.5 was found to produce little effect on the simulated deposit patterns at distances $>5R_s$ where most samples were collected. Consequently, the inversion of VMD is performed under fixed z_b, z_t, and R_s (Table 2) at 1 km height increments, so that the total number of unknowns of the discrete problem (10) is $J = 10$ and $J = 14$ in the KZ11 and BZ06 simulations, respectively.

Particle subpopulations We simulate F-particles from 63 to 1000 μm (63–500 μm) size range for the KZ11 (BZ06) ashfall and A-particles from 125 to 0.5 μm to provide mixed settling conditions for individual ash particles in the transient range of 63–125 μm where aggregation efficiency exhibit strong variation with particle size (Schumacher 1994; Gilbert and Lane 1994; James et al. 2003) (Table 3).

In our simulations, we neglect for simplicity any possible variations of free particle shape and density with respect to particle size within a given F-subpopulation. The density of simulated free particles is set to the value of the midpoint of the corresponding bin assuming a size-density relationship $\rho \propto -\log d$ (Wohletz et al. 1989; Bonadonna et al. 2002) in the 16–2000 μm size range. A constant density of 2600 kg m^{-3} is assumed for particles ≤ 16 μm, approximating the density of the solid phase of the ejecta (Proussevitch and Sahagian 2012). The density of ash particles ≥ 2000 μm is set at 1600 and 1900 kg m^{-3} for the KZ11 and BZ06 eruptions, respectively, based on our measurements of densities of large pyroclasts collected within proximal areas of recent tephra falls from these volcanoes.

Collection of ash particles from the simulated ashfalls shows a variety of angular to sub-rounded shapes characterized by different elongation (b/a) and flatness (c/b) values, where a, b, and c are the maximum, intermediate, and minimum diameters, respectively. Using projected area images, we calculate the aspect ratio $AR = a/b$ of individual particles from 63 to 125 μm and 125–250 μm size bins based on manual measurements of the corresponding Feret diameters (Riley et al. 2003). The measured ARs are found to follow approximately the gamma distribution (Fig. 4):

$$f(x;\alpha,\beta) = \beta^{\alpha}\left(\Gamma(\alpha)\right)^{-1} x^{\alpha-1} e^{-\beta x}, \qquad x = AR{-}1. \tag{14}$$

It is then assumed that the empirical distribution of the particle three-dimensional aspect ratio $AR^* \equiv F^{-1} = a/\left[\frac{1}{2}(b+c)\right]$ can be approximated to a reasonable accuracy by $f(x^*;\alpha^*,\beta^*)$, where $x^* = AR^* - 1$ and α^* and β^* are unknown coefficients, so that $f(x^*;\alpha^*,\beta^*) \rightarrow f(x;\alpha,\beta)$ in the asymptotic limit $c/b \rightarrow 1$. Using the general rule for transforming probability density functions along with the definition of AR^*, we obtain

$$u(F) = \frac{1}{F^2} f\left(\frac{1}{F} - 1, \alpha^*, \beta^*\right), \tag{15}$$

where $u(F)\,\partial F$ gives the relative number of particles in a range from F to $F + \partial F$. For each size bin, we use a trial set of $P = 3$ model subpopulations distributed according to Eq. (15), with the corresponding modal values F_{mod} at 0.4, 0.55, and 0.8 (Fig. 4) (we refer to these subpopulations as $F_{0.4}$, $F_{0.55}$, and $F_{0.8}$, respectively). A low value for the scale parameter $\beta^*(=2)$ is accepted in final computations so that the above distributions are sufficiently flat, in accordance with the observed wide range of particle shapes according to Zingg's classification (Wilson and Huang 1979).

To constrain settling rates of ash aggregates, we consider sets of A-particles in a range of size bins from $k = 0$ to $k = 4$ (based on diameter d_a), with each set divided into the three subpopulations of particles having constant densities ρ_a of 250, 500, and 1000 kg m^{-3} to obtain the total number of $Q = 15$ A-subpopulations. The associated range of fall velocities of A-particles overlaps those of natural ash aggregates, generated by electrostatic forces in the presence of variable amounts of atmospheric water, constrained by direct observations of ashfalls (Carey and Sigurdsson 1982), laboratory measurements (James et al. 2002, Fig. 5), and the results of model simulations (see Mastin et al. 2016, and references therein).

Table 2 List of model parameters used in forward and inverse simulations

Model parameters	Source
Input (fixed) parameters:	
1 × 1° meteorological fields (initial and boundary conditions)	NCEP FNL
Model particle subpopulations ($S_{k,\,p}$): see Table 3	
Volcanic source height range (z_b, z_t):	
z_b = 1.5 km, z_t[a] = 11.5 km (KZ11 simulations)	Seismic data[b]
z_b = 2.0 km, z_t[a] = 16.0 km (BZ06 simulations)	Girina (2013)
Forward simulations	
RAMS-simulated meteorological fields	
λ_x, λ_y bandwidth parameters calculated according to the turbulence model	Yamada and Bunker (1988)
HYPACT-derived source functions ($g_{k,\,p,\,j}$)	
Adjustable parameters	
The source radius (R_s)[c]	
8–20 km (BZ06 simulations)	
4–20 km (KZ11 simulations)	
Optimal subset of particle subpopulations (see Table 3)	
Inversion parameters	
The best-fit subsets (S_k^*) for each size bin of grain-size analyses	
Source mass parameters: TEM, TGSD, VMD	

[a] A plausible upper limit on ash injection altitudes

[b] Based on visual inspection of seismic data and quantitative comparison with other eruption events of similar magnitude

[c] The plausible ranges of R_s. The finally accepted values are R_s = 12 km and R_s = 8 km in the BZ06 and KZ11 simulations, correspondingly

The power law size distribution $n(l) \propto l^{-D}$ is used for particles in each model subpopulation, where $n(l)\partial l$ is the number of either free particles ($l \equiv d$) or aggregates ($l \equiv d_a$) between l and $l + \partial l$. We set $D = 4$ based on results of trial simulations so that the total mass of ash in a given subpopulation $S_{k,\,p}$ is uniformly distributed over $\phi \in [k, k-1]$ ($\phi = -\log(l/l_0)$, $l_0 = 2$ mm) (see Wohletz et al. 1989, Eqs. (4, 5, and 34)). The whole set of trial F- and A-subpopulations, each represented by $I_p = 32{,}000$ HYPACT particles, is summarized in Table 3. An orthogonal sampling method (McKay et al. 1979) is used to achieve a nearly uniform initial spatial distribution of the emitted particles over the whole volume of each model emission source (Ω_j).

Source functions The results of HYPACT simulations were used to calculate the source function values $g_{k,\,p,\,j}(\mathbf{r}_i)$, $i = 1, I$, using the density kernel approach (Rosenblatt 1956; De Haan 1999):

$$g_{k,p,j}(\mathbf{r}_i) = \sum_{n=1}^{Ip} \left(m_{k,p,j}\right)_n \cdot K\left(|x_n - x_i|/\lambda_x, |y_n - y_i|/\lambda_y\right), \qquad (16)$$

where $(m_{k,\,p,\,j})_n$ is a mass of the nth model particle related to the subpopulation $S_{k,\,p}$ and the source Ω_j, x_n, y_n are particle coordinates on the Earth's surface, $K(\cdot)$is a kernel function, and λ_x, λ_y are bandwidth parameters controlling the area over which m_n is spread through unresolved motions. A physical concept of

Table 3 Model F- and A-subpopulations used in the simulations ($P + Q$ is the total number of trial subpopulations per size bin)

Ash particle size bins, k	Ash particle size range, μm	Model F-subpopulations	Model A-subpopulations	$P + Q$
KZ11 event				
1, 2, 3	125–1000	$F_{0.4}$, $F_{0.55}$, $F_{0.8}$	–	3
4	63–125	$F_{0.4}$, $F_{0.55}$, $F_{0.8}$	A_1–A_{15}	18
5–11	0.5–63	–	A_1–A_{15}	15
BZ06 event				
2, 3	125–500	$F_{0.4}$, $F_{0.55}$, $F_{0.8}$	–	3
4	63–125	$F_{0.4}$, $F_{0.55}$, $F_{0.8}$	A_1–A_{15}	18
5–11	0.5–63	–	A_1–A_{15}	15

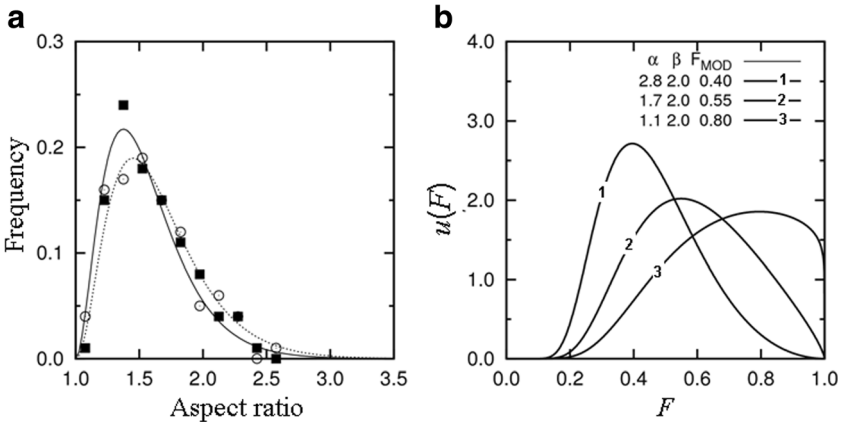

Fig. 4 **a** Aspect ratio (length/width) of ash particles in the 63–250 μm size range from the KZ11 (squares) and BZ06 (circles) ashfalls and the best-fit beta distribution curves to empirical data: $\alpha = 3$, $\beta = 5.4$, *AR* (mode) = 1.37 (KZ11, solid line), $\alpha = 3.2$, $\beta = 4.9$, *AR* (mode) = 1.45 (BZ06, dashed line). **b** Particle shape distributions $u(F)$ (solid curves 1–3) in F-subpopulations as a function of Wilson and Huang's shape factor F

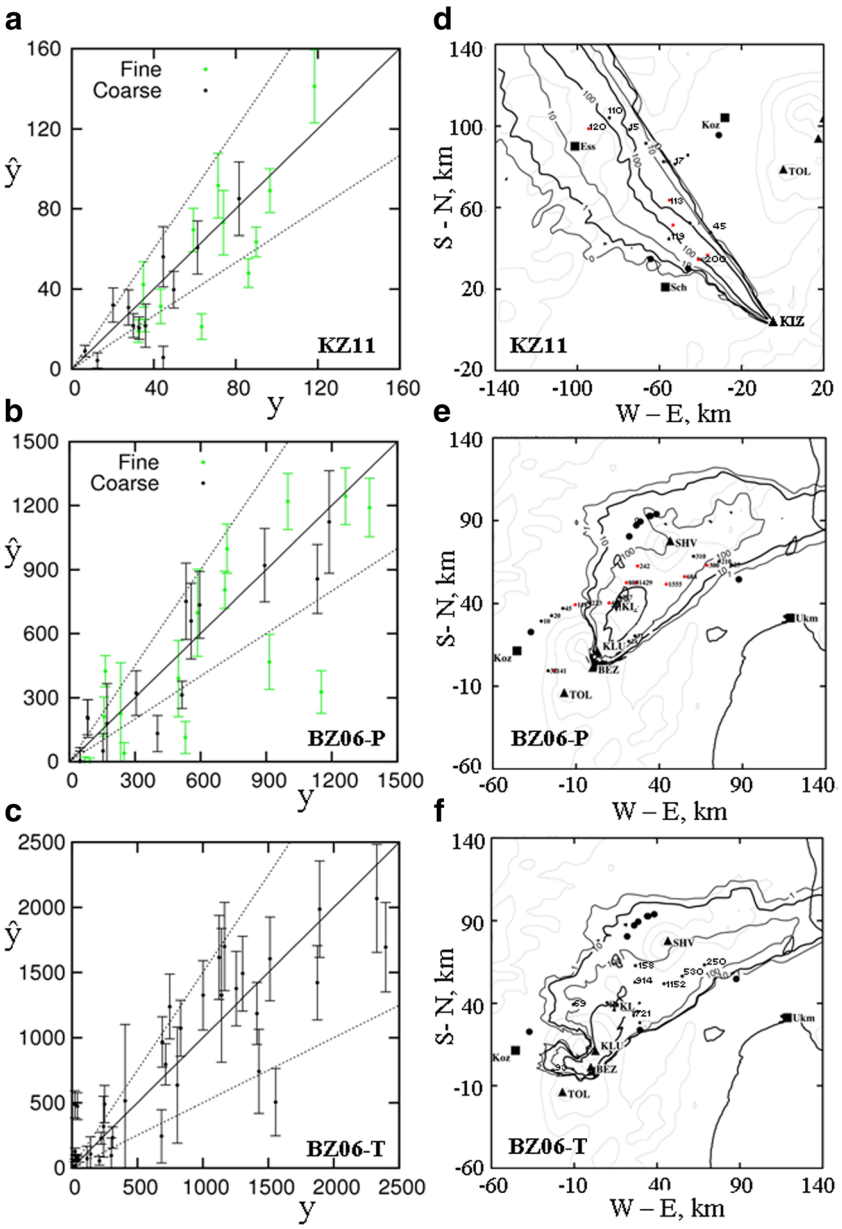

Fig. 5 **a**–**c** Plots of the observed (y) vs. calculated ($\hat{y}$) mass loads, g m^{-2}. Vertical bars indicate ± 2 standard error interval for the corresponding estimate. Dashed lines mark the area within which a predicted value lies within a factor of 1.5 of the observed value. **d**–**f** Model-predicted deposit maps (g m^{-2}) (G3 computational grid). Numbers in figures show MPA value measured at each location. Volcanoes (also shown in Fig. 1): KIZ, Kizimen; BEZ, Bezymianny; SHV, Shiveluch; TOL, Plosky Tolbachik

turbulent dispersion of individual puffs in a far-field limit (De Haan and Rotach 1998) is used to prescribe a Gaussian-shaped kernel estimator K whose bandwidths are determined, as part of the upgraded numerical algorithm of HYPACT, through time integration of the velocity variances along a parcel trajectory (see Yamada and Bunker (1988) for further discussion).

Simulation scenarios

In the case of the KZ11 data set, we have $I = I_g$, so that the fraction-based approach is directly applied to invert VMD, TGSD, and TEM of ash particles emitted from the whole range $[z_b, z_t]$ of injection heights. Two types of simulations are performed for the BZ06 ashfall. Since the BZ06 grain-size samples were collected only within the Plinian part of the deposit, the fraction-based approach is applied to invert the source mass parameters within the probable range of heights of the umbrella cloud (i.e., 8–15 km). The bulk ash-based approach is also used to derive VMD and TEM of ash for the whole range of injection heights based on the complete set of mass per area samples (Table 1). We refer to the above simulations as BZ06-P (Plinian) and BZ06-T (total) simulations.

Since a direct estimation of the model error covariance matrixes is strongly inhibited by the small amount of data and unknown distribution of the model prediction errors, we adapt the simplest form for $\mathbf{W}$ and $\mathbf{W}_k$ by setting $w_{i,j} = (w_{i,j})_k = \delta_{i,j}$ (where $\delta_{i,j}$ is a delta function) in the KZ11 and BZ06-P simulations. The above approach was found to be better than alternative techniques based on proportional weighting factors ($w_{i,i} = 1/y_i^2$) or statistical weighting ($w_{i,i} = 1/y_i$), as shown by the respective residual plots (Draper and Smith 1998). This feature may be indicative of the complex nature of the prediction errors whose magnitudes are not directly related to the measured mass loads, but instead by a variety of atmospheric and depositional factors acting on sub-grid scales (Engwell et al. 2013).

In the BZ06-T simulations, there is a marked difference in the measured mass loads from the Plinian ($\langle y \rangle = 947$ g m^{-2}) and co-PF ($\langle y \rangle = 73$ g m^{-2}) parts of the deposit, where $\langle y \rangle$ is the mean observed mass load for the corresponding subset of samples. The proportional weighting factor ($w_{i,i} = 1/\langle y \rangle^2$) is then used for each of the above subsets to balance their contribution into the TSVD-based optimal solution.

Inversion results

As statistical measures to describe the model performance, the relative root mean square difference $\mathrm{rRMSD} = \left(I^{-1}\sum_{i=1}^{I}\varepsilon_i^2\right)^{1/2}/\bar{y}$ and the overall relative bias ($\mathrm{ORB} = (I\bar{y})^{-1}\sum_{i=1}^{I}\varepsilon_i$) are determined, where $\bar{y} = I^{-1}\sum_{i=1}^{I} y(\mathbf{r}_i)$ is a mean observed mass load and $\boldsymbol{\varepsilon} \equiv \mathbf{y} - \hat{\mathbf{y}}$ is a vector of residuals (see Eq. (7)). We obtain rRMSD = 0.46, ORB = 0.13, $\bar{y}$ = 37.3 g m^{-2} and rRMSD = 0.42, ORB = 0.12, $\bar{y}$ = 67.1 g m^{-2} for the KZ11 coarse and fine ash fractions and rRMSD = 0.48, ORB = 0.02, $\bar{y}$ = 761.9 g m^{-2} for the BZ06-T bulk ash simulations. According to Fig. 5a–c, the majority of the predictions fall within a factor of 1.5 of the measured mass loads, with a few outliers resulting from large prediction errors near the deposit margins where spatial gradients of the mass load are greatest (Fig. 5d–f). It is important to note the low ORB values despite some high rRMSDs reaching ~ 50% of the mean of the observed mass loads. The low ORBs, along with the absence of any meaningful trends in the residuals with respect to distance from vent and azimuth angle (Fig. 6), indicate the general adequacy of the derived fits (Draper and Smith 1998) and correct estimation of the particle fall velocity spectrum.

The VMDs of ash from the KZ11 and BZ06-T simulations (black solid lines) and the BZ06-P simulation (black dashed line) are shown in Fig. 7. The close proximity of the two BZ06 VMDs at heights > 8 km is due to the above mentioned specifics of the BZ06 data set as the co-PF cloud-related subset of measurements does not affect the results of the BZ06-T simulations for the upper part of the eruption column. The derived total VMDs show a distinct multimodal structure resulting from the complex character of the eruption source. The upper tropospheric and lower tropospheric parts of the VMDs reflect a contribution of ash injected from the umbrella cloud which developed in the vicinity of and well above the neutral buoyancy level (z_u) of the vent-originated eruption plume. The model-predicted heights z_u, which we associate with the primary peaks in the derived VMDs, are 6 km in the KZ11 simulations and 11.5 km in the BZ06-F and BZ06-T simulations. The above values are ~ 1–2 km higher than the observed heights of the downwind plumes (5–6 km and 9–10 km, respectively, see section "Volcanological setting"). The observed discrepancy is most probably due to the expected overall descent of the ash plume en route, with the corresponding travel times of 20 min in the KZ11 event and > 30 min in the BZ06 event based on the observed wind speeds at these levels (atmospheric sounding data from http://weather.uwyo.edu/upperair/sounding.html).

Figure 7 also shows the proportion of fine ash ($(m_{63})_j$ values) within the altitude ranges of the fraction-based simulations (green solid lines). According to the figure, gravitational separation of particles at heights $\geq z_u$ results in a rapid decrease in coarse ash abundance, likely due to a rapid decrease in vertical plume speed in the upper part of the eruption plume (see Fig. 4 from Moiseenko and Malik (2014) for the vertical speed profile in the BZ06 eruption column simulated with PlumeRise model). The respective proportion of fine ash increases from 0.63 (z = 5 km) to ~ 1.0 (z > 10 km) for the KZ11 event, and from 0.47 (z = 10.5 km) to 0.85 (z = 15 km) for the BZ06 event. The lower fine ash proportions in the BZ06-P simulations are likely due to the coarser GSD of the Plinian fall ash as well as more energetic motions in the BZ06

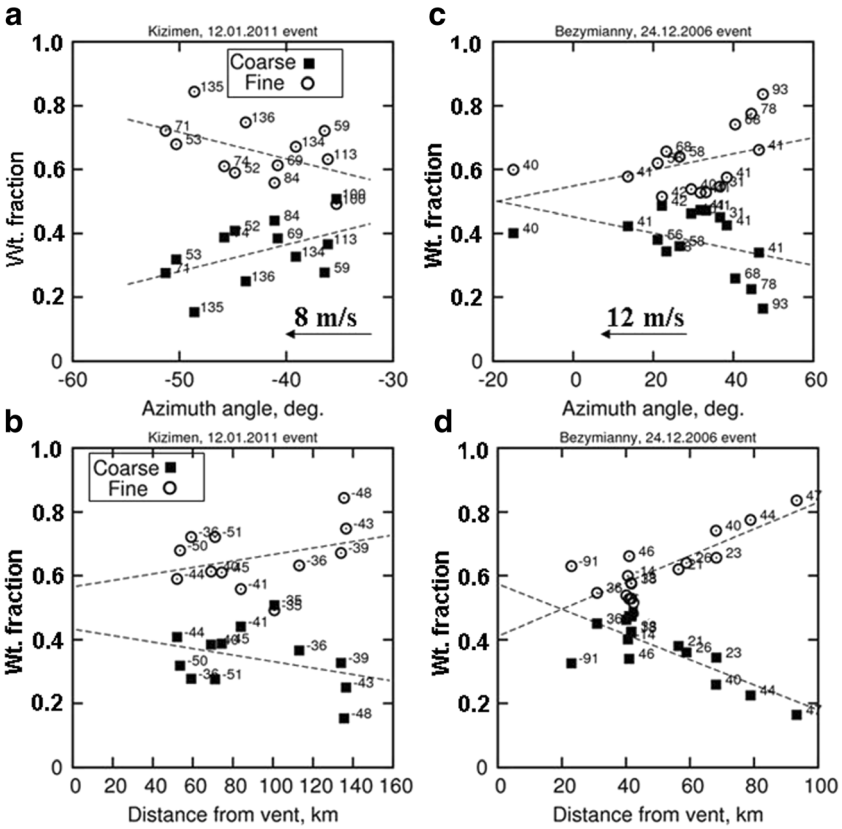

Fig. 6 The observed (markers) and simulated (regression lines to model-predicted values) changes in fine and coarse ash fractions from the KZ11 (**a**, **b**) and BZ06 (**c**, **d**) fall deposits as a function of azimuth angle (counted from the north) (**a**, **c**) and distance (**b**, **d**) relative to the vent. Subscripts on the graphs are distances from the vent (**a**, **c**) and azimuth angles (**b**, **d**). The direction of low-level (< 500 m a.g.l.) wind in **a** and **c** is shown by the arrow

umbrella cloud which could have meant that turbulent mixing still dominated the gravitational sorting of the sub-millimeter particles at the time of the BZ06 Plinian ash fallout.

The VMDs from the KZ11 and BZ06 simulations show distinct secondary maxima at heights well below z_u, which can be explained by a significant contribution of ash from the co-PF clouds. In particular, the height of the secondary peak from the BZ06 VMD (5.5 km) is in close agreement with the predicted top height of the co-PF clouds (of ~4.5–5.3 km) based on the empirical relationship, $h_t = 8 - 10\ h_F$, for Bezymianny Volcano (Girina 1998) (h_t is a co-PF cloud top height above ground level, h_F is a width of the pyroclastic flow at its frontal part; $h_F = 425$ m in the present case). There is an appreciable contribution of the co-PF ash in the KZ11 event as well, which is clearly seen from the predicted fines-enriched ($m_{63} = 0.74$) secondary maximum peaking at 4 km. The above feature is in agreement with the observed strong pyroclastic flows accompanying all the current explosive activity at the volcano.

The estimated TEMs of the coarse and fine ash fractions are $0.31 \pm 0.05 \times 10^9$ kg and $0.90 \pm 0.10 \times 10^9$ kg (the KZ11 event, particles ≤ 1000 μm) and $0.93 \pm 0.16 \times 10^9$ kg and $1.27 \pm 0.17 \times 10^9$ kg (the BZ06 Plinian fall, particles ≤ 500 μm). The derived proportion of fine ash from the BZ06 umbrella cloud ($m_{63} =$

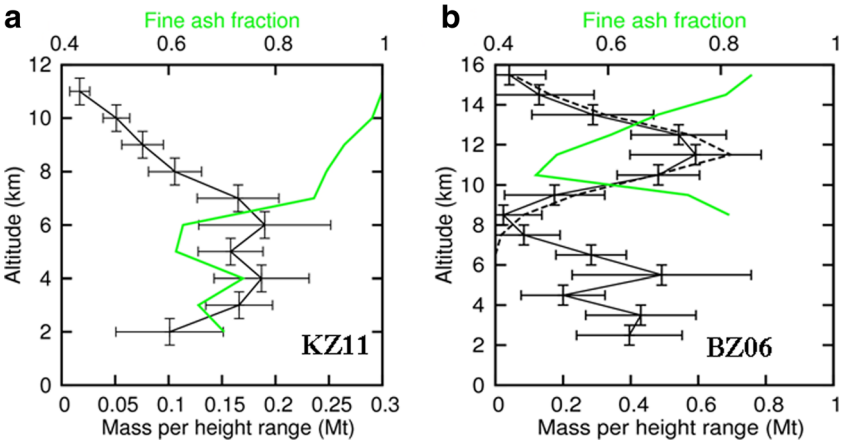

Fig. 7 **a**, **b** Vertical ash mass distribution (black) and fine ash proportion (m_{63} value) (green) from the emitted ash for the KZ11 and BZ06-T simulations (the fraction-based approach) (Mt=10^9 kg). Horizontal bars indicate ± 2 standard error interval for the corresponding estimates. Vertical bars mark the respective height range for each estimate. The dashed line in **b** is the VMD of ash for the BZ06-P simulations (the bulk ash-based approach)

Table 4 Best-fit model subpopulations for the simulated size bins. Values in columns 3–5 relate to the parameters of individual ash particles and aggregates for F and A settling mode, respectively. In the case of the two best-fit subpopulations (bins 4 and 5–11 in the BZ06 event), their respective mass fractions are provided in the second column

Size bin	Settling mode	Size range[a], μm	Average density, g cm^{-3}	Shape factor F[b]	v_t range, m/s
			KZ06 event		
1	F	500–1000	1.81	0.55	1.53–5.26
2	F	250–500	1.96	0.55	0.70–3.38
3	F	125–250	2.10	0.8	0.19–1.84
4	F	63–125	2.24	0.4	0.06–0.82
5–11	A	63–125	1.00	1.	0.12–0.47
			BZ06 event		
2	F	250–500	2.15	0.55	0.73–3.81
3	F	125–250	2.25	0.8	0.26–2.28
4	F (0.65)	63–125	2.35	0.8	0.08–1.00
	A (0.35)	250–500	0.50	1.	0.76–1.95
5–11	A (0.25)	250–500	0.25	1.	0.42–1.22
	A (0.75)	250–500	0.50	1.	0.76–1.95

[a] Size range of individual ash particles and aggregates in the case of F and A settling modes, correspondingly

[b] The mode of the distribution (15) for F-particles

0.58) is significantly lower compared to that from the KZ11 deposit ($m_{63} = 0.75$) which may reflect the different rheology of the erupting magma in typical vulcanian and sub-Plinian style eruptions (Walker 1981; Cas and Wright 1987). We note that the observed high abundance of fine-grained particles in the KZ11 fall deposit is a common feature of ashfalls produced by the volcano during its current explosive activity. According to BZ06-T simulations, the TEM of particles ≤ 500 μm is 4.16 ±

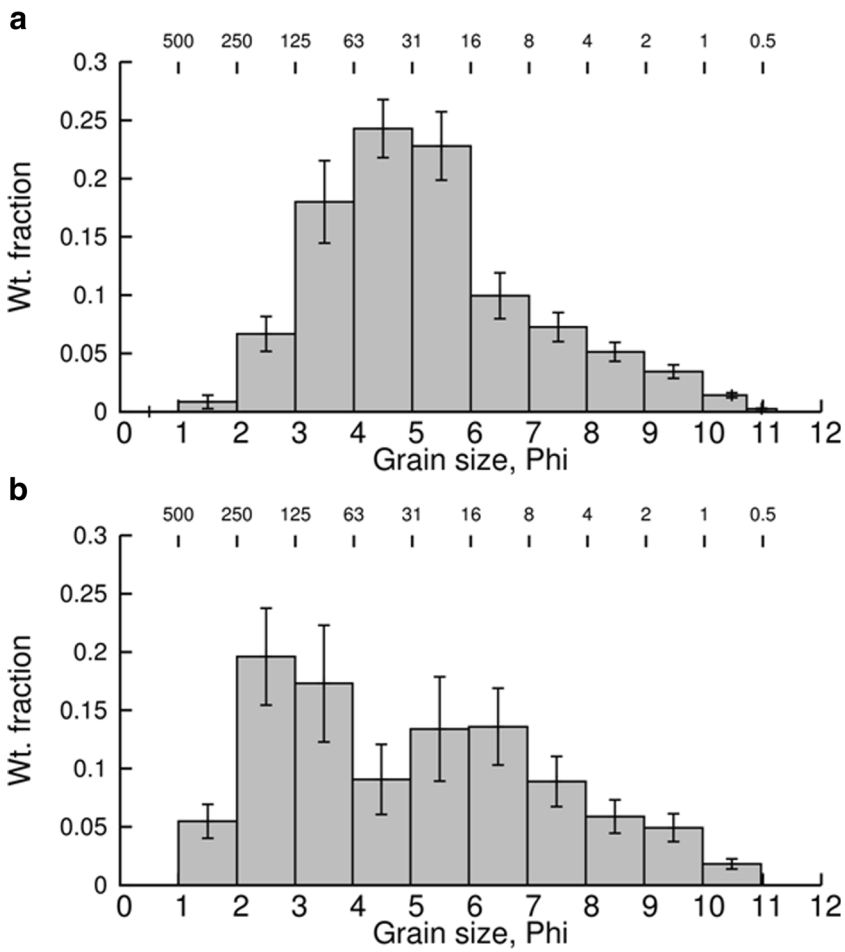

Fig. 8 The model-retrieved TGSD (± 2 standard error) of ash particles from the KZ11 ashfall deposit (eruption cloud and Co-PF plumes) (**a**) and the BZ06 Plinian fall deposit from the umbrella cloud (**b**)

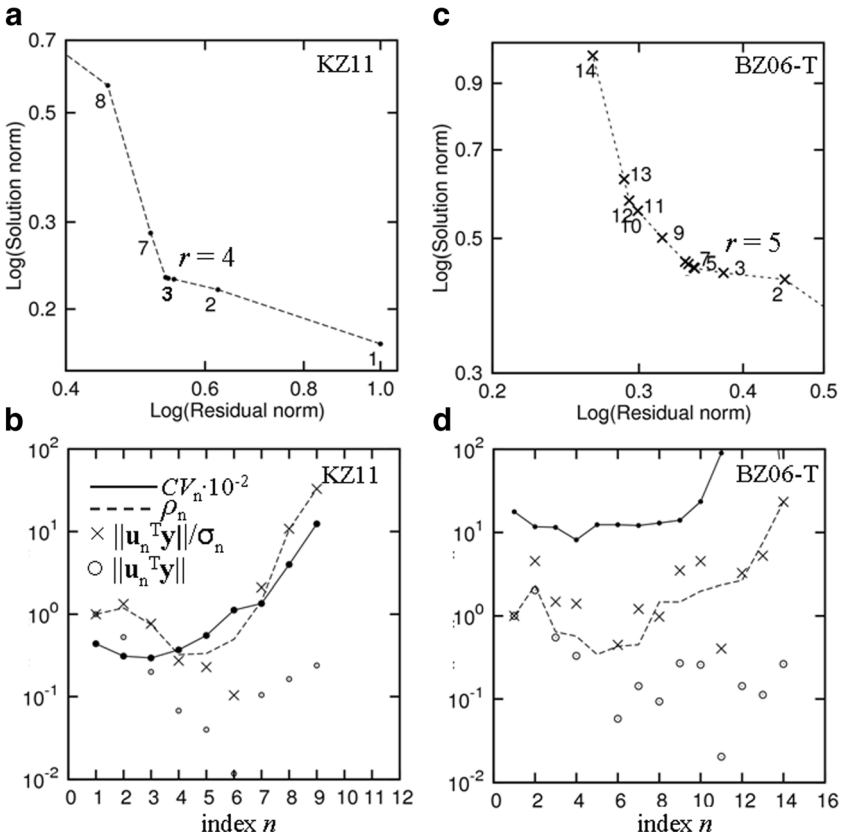

Fig. 9 The L-curves (**a**, **c**) and plots of ρ_n, $|\mathbf{u}_n^T\mathbf{y}|$, and CV_n (**b**, **d**) for the KZ11 fine ash and BZ06-T bulk ash simulations. The *r*s are optimal truncation numbers

0.58×10^9 kg, of which $2.32 \pm 0.48 \times 10^9$ kg was injected at heights of the umbrella cloud. The derived TEMs from the KZ11 and BZ06 ashfalls agree well with independent estimates provided above in section "Volcanological setting."

The best-fit subpopulations of ash particles in the KZ11 and BZ06-P simulations are shown in Table 4. In most cases, a single subpopulation of either F- or A-particles is required to approximate FVD within the given size range. The only exception is the mixed settling regime of ash particles from the BZ06 63–125 μm size bin and aggregate settling regime of the BZ06 fine ash mode (particles ≤ 63 μm) simulated with the two best-fit subpopulations. Also, the model-predicted high modal values of the shape factors (0.55–0.8) (Table 4) are in quantitative agreement with a visual examination of ash particles from the KZ11 and BZ06 samples, which shows a high abundance of equant to sub-equant shapes (Guschenko 1965).

The transition from free to aggregate/mixed settling regime is predicted for particles ≤ 63 μm and ≤ 125 μm for the KZ11 and BZ06 ashfalls, respectively. Previous studies demonstrate that the exact threshold size separating the free particle and aggregate-dominated settling regimes varies across a broad range from a few tens to hundreds of microns depending on the amount of accessible liquid water (Gilbert and Lane 1994; Schumacher 1994; Schumacher and Schmincke 1995). Dryer environmental conditions in the KZ11 eruption event resulted in a sharp transition between the two settling modes, lower threshold size, and narrower range of aggregate settling speeds compared to the respective values for the BZ06 Plinian fall (see Table 4). The settling speeds of aggregate particles in the BZ06 ashfall were in the range of 0.42–1.95 m s^{-1}, with optimal values for effective aggregate sizes and densities being 250–500 μm and 0.25–0.5 g cm^{-3}, respectively. The proposed ranges are similar to those derived from numerical simulations of ashfall from the May 18, 1980, Mt. St. Helens eruption (V_t = 0.7–0.8 m s^{-1}, ρ_a = 400–600 kg m^{-3}, d_a = 0.2–0.3 μm) (Folch et al. 2010; Mastin et al. 2016), thus supporting results of previous simulations according to which aggregation of fine ash operates as a discrete process that is not directly related to eruption style or magnitude (Mastin et al. 2016).

The model-derived TGSDs from the KZ11 fall deposit and the BZ06 Plinian fall deposit are shown in Fig. 8. Bonadonna and Houghton (2005) demonstrate that TGSDs obtained from some common sedimentological techniques are highly dependent on the availability of samples from the most proximal and distal parts of the deposit. Since the deposit data are used to constrain FVD of the initial population of ash particles in the present simulations, incomplete sampling could also have an impact on successful inversions unless the ash transport and deposition conditions are approximately uniform across the whole deposit dispersal area. Consequently, the TGSDs calculated in this study must be considered only as indicative,

and representative of some of the most important features of the true size distribution. The model-predicted TGSD of the KZ11 ashfall is unimodal, peaking at 5Φ (31–63 μm size bin), and probably representative for particle size distribution in the eruption column, with a small addition of the elutriated fine ash. The observed unimodality was found to be a common feature of other ashfall deposits from vulcanian type explosions and rock fragments produced in shock-tube experiments on rapid decompression at high temperatures (Spieler et al. 2003). The predicted bi-modal structure of the TGSD of the BZ06 Plinian fall most probably reflects a size selective aggregation process, which plays an appreciably more significant role in the BZ06 fallout compared to that from the KZ11 event. As noted by Schumacher (1994), the existence of a grain-size boundary separating fine *cluster-forming* ash from coarser *cluster-modified* ash particles (using the author's notation) somewhere in a range of 45–63 μm leads to a distinct minimum in grain-size distribution in intermediate parts of the deposit (Durant and Rose 2009; Rose and Durant 2009). This is frequently observed in Plinian and sub-Plinian fall deposits (see more references in Schumacher (1994)) and is also supported by the results of the BZ06 Plinian fall simulations.

Discussion and conclusions

Explosive volcanic eruptions generate large amounts of ash particles whose settling rates are not related uniquely to particle size or mass owing to a wide range of shapes and densities and aggregation processes. The proposed inversion approach, which is based on a trial set of particle subpopulations, allows the probable ranges of particle aerodynamic parameters to be constrained; these parameters vary depending on the fall velocity model selected. Results show that the predicted eruption source parameters are generally consistent with the spatial characteristics of the actual deposit dispersal pattern, measured grain-size composition, and observational constrained height of the eruption column. It might be supposed that the obtained low signal-to-noise ratio ($\overline{y}/\sigma_0$ value) (2.4 and 2.1 for the KZ11 and BZ06-T simulations, respectively) is created by this inversion technique owing to the specifics of the measurement data and limitations in the atmospheric modeling. However, we demonstrate that the TSVD-based inversion technique is able to provide physically meaningful results even where there are large uncertainties in the ash transport simulations.

When emitted into the atmosphere, volcanic ash particles are entrained by atmospheric movements over an extremely wide range of spatial and temporal scales, contributing to the total effect of differential advection and turbulent dispersal of the eruption cloud. Temporal evolution of ash plumes at substratospheric heights is known to be strongly controlled by mesoscale (2–2000 km) atmospheric processes and is the region of the total spectrum of atmospheric motions that is mainly stochastic in nature and hence can be predicted only in a statistical sense. The potential role of errors in simulating the evolution of ash plumes on a mesoscale is expected to be quite large for those vulcanian and sub-Plinian type eruptions which are too short-lived relative to the tropospheric Lagrangian time $T_L \sim f^{-1}$ (~10^4 s in the mid-latitudes) of the energy-containing eddy motions estimated from the Coriolis parameter f (Gifford 1984; Mikkelsen et al. 1988), which is the case in this study. Our simulations strongly indicate that careful selection of the model parameters which affect the rate of horizontal dispersion (i.e., the volcanic source radius R_s and the bandwidth values λ_x, λ_y in Eq. (16)) is a necessary prerequisite for obtaining consistent results for the eruption parameters and the predicted deposit dispersal pattern.

In our computations, we employ the method of Yamada and Bunker (1988) for calculating optimal bandwidths based on the RAMS sub-grid turbulence and Taylor's (1921) homogeneous diffusion theory. This provides a physically meaningful alternative to a widely used approach based on the treatment of the turbulent dispersal rate as an adjustable parameter of the inversion procedure. Consequently, the only adjustable parameter affecting the horizontal dimensions of the downwind plume in our simulations is R_s which must be considered as an effective radius of the eruption cloud near the source (see Gifford 1955, 1984). Using well-developed approaches to find an optimal truncation number for the TSVD solution thus provides an objective control on the degree of model prediction error due to both unknown settling rates and limitations of atmospheric transport simulations.

An appreciable contribution of both the umbrella region and co-PF clouds into the simulated ashfall deposits is clearly seen in the fact that the derived VMDs peak at the height of the downwind ash plume with strong secondary maxima at lower tropospheric levels. The general conclusion is that the proposed inversion technique is able to provide additional insight into the vertical ash mass distribution and gravitational separation of ash particles in an eruption column provided the amount of field data is sufficient to resolve the fine spatial structure of the eruption source.

Important limitations of the current inversion approach arise from neglecting temporal variations in volcanic source geometry, eruption intensity, and the ash particle settling regime. Using observational data for the above parameters in inverse simulations is an interesting challenge as it would allow for better quantification of the atmospheric and volcanological factors affecting ash dispersal and fallout on a regional scale.

Acknowledgements We thank Dr. O. Girina for fruitful discussion of the related topics, as well as colleagues from IVS U. Demyanchuk, T. Manevich, Y. Muravyev, A. Ovsyannikov, I. Tembrel, and A. Sokorenko who took part in sample data collection and analyses during

the 2006 and 2011 field works on Bezymianny and Kizimen volcanoes. We also thank anonymous reviewers for their valuable suggestions and comments that helped to improve the original manuscript as well as A. Harris, C. Bonadonna, and F. Van Wyk de Vries for editorial handling.

Appendix 1. Basic notations

Variable	Definition
R	Initial population of the erupted ash particles
Ω_j	jth model emission source
k	2^{-k}–2^{-k+1} mm size bin
$S_{k,p}$	A model pth subpopulation of particles in kth size bin
R_{mod}	A set of model particle subpopulations $S_{k,p}$
F, A	Model classes of free particles and ash aggregates
$y(\mathbf{r}_i)$	Mass per area at sample site $\mathbf{r}_i$ [ML^{-2}]
$\boldsymbol{\varepsilon}$	Vector of model prediction errors [ML^{-2}]
$\gamma_{k,p,j}$	Total mass of $S_{k,p}$-particles emitted from jth model source [M]
$g_{k,p,j}(\mathbf{r})$	Value $y(\mathbf{r})$ corresponding to $\gamma_{k,p,j} = 1$ [ML^{-2}]
a, b, c	Particle axial lengths, $a > b > c$ [L]
AR	Aspect ratio a/b, dimensionless
F	Shape parameter $= (b + c)/(2a)$, dimensionless
AR^*	Inverse of the shape parameter ($= F^{-1}$), dimensionless
α, β	Coefficients of the beta distribution
q	Vertical ash mass distribution [ML^{-1}]
z_b	Vent altitude [L]
z_t	The top height of the eruption column [L]
R_s	Radius of model emission source [L]
M_{tot}	Total erupted mass (TEM) of ash particles [M]
ΔM_k	TEM of particles in a size bin k [M]
M_j	TEM of particles emitted from jth model source [M]
$\xi_{k,p}$	Weight fraction of $S_{k,p}$-particles in TEM, dimensionless
m_{63}	Weight fraction of fine ash ($\leq$ μm) particles in TEM, dimensionless
v_t	Settling speed of either individual particle or ash aggregate [LT^{-1}]

Appendix 2. The inversion technique

In practical calculations a straightforward method of solution to linear systems (8, 10) is strongly inhibited by ill-conditioning of the matrixes $\mathbf{A}_k$ and $\mathbf{B}$. Additionally, the amount of measurement data involved is commonly greatly insufficient for a prior estimation of the covariance matrix $\mathbf{W}$ for the observations, which places important limitations on choosing solution methods. An optimal, in a least squares sense, solution to Eq. (8) is obtained via a subset selection process which is the natural method of regularization to the corresponding least squares problem according to the general representation (5) (see further discussion in Moiseenko and Malik (2014)). A truncated SVD (singular value decomposition) technique (Varah 1973; Hansen 1990a, 1990b) is used as a regularization method for solution to Eq. (10). Following (Varah 1973), the SVD of the problem matrix $\mathbf{B}' = \mathbf{WB}$is defined as

$$\left(\mathbf{B}'\right)_{I\times J} = \mathbf{U}_{I\times I}\Sigma_{I\times J}\mathbf{V}^T_{J\times J}, \quad \Sigma = \mathrm{diag}(\sigma_1, ..., \sigma_J) \qquad (17)$$

where $\mathbf{U}$ is an orthogonal matrix whose column vectors $\mathbf{u}_1$, ..., $\mathbf{u}_I$ span the vector space of the data, $\mathbf{V}$ is an orthogonal matrix whose column vectors $\mathbf{v}_1$, ..., $\mathbf{v}_J$ span the vector space of unknowns, and diag denotes a diagonal matrix with diagonal elements equaling to singular values of $\mathbf{B}'$ arranged in the decreasing order: $\sigma_1 \geq \sigma_2 \geq ... \geq \sigma_J > 0$. The truncated SVD (TSVD) solution $\mathbf{m}_r$ to Eq. (10) is given as a weighted sum of the first r singular vectors $\mathbf{v}_n$ ($n = 1, ... r$):

$$\mathbf{m}_r = \sum_{n=1}^{r} \frac{\mathbf{u}_n^T \mathbf{y}'}{\sigma_n}\mathbf{v}_n, \qquad (18)$$

where $\mathbf{u}_n^T\mathbf{y}'$ is an nth Fourier coefficient of the expansion of the transformed observation vector $\mathbf{y}' = \mathbf{Wy}$ in the data space, and r is the truncation parameter of the expansion.

According to the general properties of an atmospheric transport operator (with $\mathbf{B}$ as an example, see Eq. (11)), the number of oscillations in the left and right singular vectors $\mathbf{u}_n$ and $\mathbf{v}_n$ increases with n, so that choosing a particular value for r provides a control on smoothness of the regularized solution $\mathbf{m}_r$. The necessary conditions for obtaining a meaningful TSVD solution are that (I) the Fourier coefficients of the problem (10) *unperturbed* by model errors decay to zero faster than the σ_n so that the discrete Picard condition (DPC) is satisfied; (II) the total amount of perturbations is bounded (i.e., the signal-to-noise ratio in the perturbed problem is not too low) (Hansen 1990b). Under the above assumptions, the both measurement data and the true VMD have small components at high n in the data and parameter spaces, correspondingly, so that a satisfactory approximate solution can be obtained by truncating SVD of $\mathbf{B}'$ at some r below its maximal theoretical value given by J.

In present simulations, the control on the propagation of model uncertainties is achieved by using several simultaneous strategies to find the optimal truncation number basing on visual examination of plots $(e_r, \|\mathbf{m}_r\|)$, $(n, \|\mathbf{u}_n^T\mathbf{y}'\|)$, and $(n, \|\mathbf{u}_n^T\mathbf{y}'\|/\sigma_n)$, where $e_r = \|\mathbf{y}' - \mathbf{B}'\mathbf{m}_r\|$ and $\|\mathbf{m}_r\|$ represent L_2 norms of the residual vector and the regularized solution, correspondingly. Particularly, the curve given by the set of points $(e_r, \|\mathbf{m}_r\|)$ is known to exhibit a characteristic L-shaped behavior in log-log scale provided the conditions (I, II) are satisfied (Hansen 1990a). The optimal regularized solution can then be computed as the solution $\mathbf{m}_r$ corresponding to the corner of the curve to achieve a good balance between the solution and residual norms (see more discussion in Hansen (1990a, 1990b, 1992)).

In practical computations, the DPC is not satisfied for those coefficients which are associated with the large singular values, as $\mathbf{u}_n^T\mathbf{y}'$ have a tendency to be dominated by model errors at high n. We then use the DPC-based approach to find the optimal truncation number by calculating the three-point moving geometrical mean (see Hansen (1990b), Eq. 5.1 with $q = 1$):

$$\rho_n = \sigma_n^{-1}\left(\Pi_{n-2}^{n+2}\,\mathbf{u}_n^T\mathbf{y}'\right)^{1/3}, \quad n = 3, ..., J-2, \tag{19}$$

and setting r equal to the index n corresponding to the first local minimum of the curve (n, ρ_n). Alternatively, the generalized cross-validation (GCV) estimate of r is computed as the global minimizer of the function $CV_n = \|(\mathbf{I} - \mathbf{B}'\,\mathbf{H}_n)\mathbf{y}'\|/(I-n)^2$ (Golub et al. 1979), where $\mathbf{I}$ is the $(I \times I)$ unit matrix and $\mathbf{H}_n$ is the pseudo-inverse of $\mathbf{B}'$ based on the first n eigenvectors of the problem matrix. We then use all the above methods (i.e., those based on the DPC, L-curve, and GCV) to check the general consistency among the inversion results obtained through different selection techniques as well as to assess the overall performance of the widely used GCV method in the present inversion problem.

To illustrate this, Fig. 9 shows various plots of TSVD solutions for the KZ11 fine ash and BZ06-T bulk ash simulations. According to the figure, the transition between the nearly horizontal part of the L-curve, where the regularization errors dominate, to the steeper, model error-dominated part at higher n occurs at $r = 4$ and $r = 5$ in the KZ11 and the BZ06-T simulations, respectively. At $n = r$, the regularization and model errors are balanced so that the above value represents the optimal truncation parameter of the problem. The essentially similar results for the optimal truncation number are obtained using the DPC-based criterion. Visual inspection of the perturbed Fourier coefficients vs. index number n (Fig. 9b, d) shows the general tendency for the perturbed Fourier coefficients $|\mathbf{u}_n^T\mathbf{y}'|$ to decrease monotonically in a range of $n \leq r$, whereas for $n > r$, they strongly fluctuate at a level dictated by model errors.

Application of the GCV method gives a lower truncation number of $r = 3$ (KZ11 simulations) and $r = 4$ (BZ06-T simulations), which results in appreciably over-smoothed solution in the former case. Inefficiency of the GCV method in the KZ11 simulations can be explained, on physical grounds, by similar transport and deposition conditions over a wide range of distances downwind, so that one could expect a high degree of correlation among the model prediction errors. As demonstrated by Hansen (1992) and Wahba (1990), formal application of the GCV approach in such circumstances may lead to unsatisfactory results due to difficulties in discriminating inputs from the true signal and a correlated noise. We finally recommend the DPC-based criterion as a primary tool for computing the optimal truncation number for a slightly overdetermined problem of the kind considered in the present study.

References

Armienti P, Macedonio G, Pareschi MT (1988) A numerical model for simulation of tephra transport and deposition—applications to May 18, 1980, Mount St Helens eruption. J Geophys Res 93: 6463–6476. https://doi.org/10.1029/JB093iB06p06463

Bonadonna C, Costa A (2012) Estimating the volume of tephra deposits: a new simple strategy. Geology 40:415–418. https://doi.org/10.1130/G32769.1

Bonadonna C, Houghton BF (2005) Total grain-size distribution and volume of tephra-fall deposits. Bull Volcanol 67:441–456 https://doi.org/10.1007/s00445-004-0386-2

Bonadonna C, Macedonio G, Sparks RSJ (2002) Numerical modelling of tephra fallout associated with dome collapses and Vulcanian explosions: application to hazard assessment on Montserrat. In: Druitt TH, Kokelaar BP (eds) The eruption of Soufrière Hills Volcano, Montserrat, from 1995 to 1999. Geological Society, London, Memoir, pp 517–537. https://doi.org/10.1144/GSL.MEM.2002.021.01.23

Bonasia R, Macedonio G, Costa A, Mele D, Sulpizio R (2009) Numerical inversion and analysis of tephra fallout deposits from the 472 AD sub-Plinian eruption at Vesuvius (Italy) through a new best-fit procedure. J Volcanol Geotherm Res 189:238–246. https://doi.org/10.1016/j.jvolgeores.2009.11.009

Carey SN, Sigurdsson H (1982) Influence of particle aggregation on deposition of distal tephra from the May 18 1980 eruption of Mount St. Helens Volcano. J Geophys Res 87:7061–7072. https://doi.org/10.1029/JB087iB08p07061

Cas RAF, Wright JV (1987) Volcanic successions: modern and ancient. Allen & Unwin, London, Boston, Sydney, Wellington xviii+528

Connor LJ, Connor CB (2006) Inversion is the key to dispersion: understanding eruption dynamics by inverting tephra fallout. In: Mader HM, Cole SG, Connor CB, Connor LJ (eds) Statistics in volcanology. Special Publications of IAVCEI. Geological Society, London, pp 231–242. https://doi.org/10.1144/IAVCEI001.18

Cornell W, Carey S, Sigurdsson H (1983) Computer simulation of transport and deposition of the Campanian Y-5 ash. J Volcanol Geotherm Res 17:89–109. https://doi.org/10.1016/0377-0273(83)90063-X

Costa A, Dell'Erba F, Di Vito M, Isaia R, Macedonio G, Orsi G, Pfeiffer T (2009) Tephra fallout hazard assessment at Campi Flegrei caldera (Italy). Bull Volcanol 71:259–273. https://doi.org/10.1007/s00445-008-0220-3

Debcedilski W (2010) Probabilistic inverse theory. Adv Geophys 52:1–102

Draper NR, Smith H (1998) Applied regression analysis, Third edn. Wiley, New York

Durant AJ, Rose WI (2009) Sedimentological constraints on hydrometeorenhanced particle deposition: 1992 eruptions of Crater Peak, Alaska. J Volcanol Geotherm Res 186:40–59. https://doi.org/10.1016/J.JVOLGEORES.2009.02.004

Durant AJ, Shaw RA, Rose WI, Mi Y, Ernst GGJ (2008) Ice nucleation and overseeding of ice in volcanic clouds. J Geophys Res 113: D09206. https://doi.org/10.1029/2007JD009064

Engwell SL, Sparks RSJ, Aspinall WP (2013) Quantifying uncertainties in the measurement of ashfall thickness. J Appl Volcanol 2:5. https://doi.org/10.1186/2191-5040-2-5

Enting IG (2002) Inverse problems in atmospheric constituent transport. Cambridge University Press, New York

Evans JR, Huntoon JE, Rose WI, Varley NR, Stevenson JA (2009) Particle sizes of andesitic ash fallout from vertical eruptions and co-pyroclastic flow clouds, Volcán de Colima, Mexico. Geology 37(10):935–938. https://doi.org/10.1130/G30208A.1

Fierstein J, Nathenson M (1992) Another look at the calculation of fallout tephra volumes. Bull Volcanol 54:156–167. https://doi.org/10.1007/BF00278005

Folch A, Costa A, Durant A, Macedonio G (2010) A model for wet aggregation of ash particles in volcanic plumes and clouds: 2. Model application. J Geophys Res 115:B09202. https://doi.org/10.1029/2009JB007176

Gifford FA (1955) Atmospheric diffusion from volume sources. J Meteorol 12:245–251. https://doi.org/10.1175/1520-0469(1955)012<0245:ADFVS>2.0.CO;2

Gifford FA (1984) The random force theory—application to meso-scale and large-scale atmospheric diffusion. Bound-Layer Meteorol 30:159–117. https://doi.org/10.1007/BF00121953

Gilbert JS, Lane SJ (1994) The origin of accretionary lapilli. Bull Volcanol 56:398–411. https://doi.org/10.1007/BF00326465

Girina OA (1991) Pyroclastic deposits of the 1984-1989 eruptions of Bezymianny volcano. J Volcanol Seismol 15:479–490

Girina OA (1998) Pyroclastic deposit from present state eruptions at andesitic volcanoes in Kamchatka region and their engineering and geological characteristics. Vladivostok, Dalnauka (in Russian)

Girina OA (2013) Chronology of Bezymianny Volcano activity, 1956–2010. J Volcanol Geotherm Res 263:22–41. https://doi.org/10.1016/j.jvolgeores.2013.05.002

Golitsyn GS, Gostintsev YA, Solodovnik AF (1989) Turbulent floating jet in a stratified atmosphere. J Appl Mech Tech Phys 30:566–577 (translated to English)

Golub GH, Heath MT, Wahba G (1979) Generalized cross-validation as a method for choosing a good ridge parameter. Technometrics 21:215–223. https://doi.org/10.1080/00401706.1979.10489751

Guschenko II (1965) Ashes of the North Kamchatka, their origins and genesis. Nauka, Moscow (In Russian)

de Haan P (1999) On the use of density kernels for concentration estimations within particle and puff dispersion models. Atmos Environ 33:2007–2021. https://doi.org/10.1016/S1352-2310(98)00424-5

de Haan P, Rotach MW (1998) A novel approach to atmospheric dispersion modelling: the puff-particle model. Quart J Roy Meteorol Soc 124:2771–2792. https://doi.org/10.1002/qj.49712455212

Hansen PC (1990a) Truncated singular value decomposition solutions to discrete ill-posed problems with ill-determined numerical rank. SIAM J Sci Stat Comput 11:503–518. https://doi.org/10.1137/0911028

Hansen PC (1990b) The discrete Picard condition for discrete ill-posed problems. BIT 30:658–672. https://doi.org/10.1007/BF01933214

Hansen PC (1992) Analysis of discrete ill-posed problems by means of the L-curve. SIAM Rev 34:561–580. https://doi.org/10.1137/1034115

Jackson DD (1972) Interpretation of inaccurate, insufficient and inconsistent data. Geophys J Roy Astr Soc 28:97–109. https://doi.org/10.1111/j.1365-246X.1972.tb06115.x

James MR, Gilbert JS, Lane SJ (2002) Experimental investigation of volcanic particle aggregation in the absence of a liquid phase. J Geophys Res 107(B9):2191. https://doi.org/10.1029/2001JB000950

James MR, Lane SJ, Gilbert JS (2003) Density, construction, and drag coefficient of electrostatic volcanic ash aggregates. J Geophys Res 108(B9):2435. https://doi.org/10.1029/2002JB002011

Klawonn M, Wolfe CJ, Frazer LN, Houghton BF (2012) Novel inversion approach to constrain plume sedimentation from tephra deposit data: application to the 17 June 1996 eruption of Ruapehu volcano, New Zealand. J Geophys Res 117:B05205. https://doi.org/10.1029/2011JB008767

Liu E, Cashman K, Rust A (2015) Optimising shape analysis to quantify volcanic ash morphology. GeoResJ 8:14–30. https://doi.org/10.1016/j.grj.2015.09.001

Malik NA (2011) The December 24, 2006 eruption of Bezymyannyi Volcano, Kamchatka. J Volcanol Seismol 5:368–277. https://doi.org/10.1134/S0742046311040051

Malik NA, Ovsyannikov AA (2011) The eruption of Kizimen Volcano in October 2010–March 2011, Vestnik KRAUNTs. Nauki o Zemle 1:7–14

Mangan TP, Atkinson JD, Neuberg JW, O'Sullivan D, Wilson TW, Whale TF, Neve L, Umo NS, Malkin TL, Murray BJ (2017) Heterogeneous ice nucleation by Soufriere Hills volcanic ash immersed in water droplets. PLoS One 12(1):e0169720. https://doi.org/10.1371/journal.pone.0169720

Marti A, Folch A, Jorba O, Janjic Z (2017) Volcanic ash modeling with the online NMMB-MONARCH-ASH v1.0 model: model description, case simulation, and evaluation. Atmos Chem Phys 17:4005–4030. https://doi.org/10.5194/acp-17-4005-2017

Mastin LG, Van Eaton AR, Durant AJ (2016) Adjusting particle-size distributions to account for aggregation in tephra-deposit model forecasts. Atmos Chem Phys 16:9399–9420. https://doi.org/10.5194/acp-16-9399-2016

McKay MD, Beckman RJ, Conover WJ (1979) A comparison of three methods for selecting values of input variables in the analysis of output from a computer code. Technometrics 21:239–245. https://doi.org/10.1080/00401706.1979.10489755

Melekestsev IV, Ponomareva VV, Volynets ON (1995) Kizimen Volcano, Kamchatka—a future Mount St. Helens? J Volcanol Geotherm Res 65:205–226. https://doi.org/10.1016/0377-0273(94)00082-R

Mikkelsen T, Larsen SE, Pecseli HL (1988) Spectral parameterization of large-scale atmospheric diffusion. In: van Dop H (ed) Air pollution modeling and its application VI. Proceedings of the 16 NATO/CCMS International Technical Meeting. Lindau, 6–10 April 1987 (NATO Challenges of Modern Society, 11). Plenum Press, New York, pp 579–591

Moiseenko KB, Malik NA (2014) Estimates of total ash content from 2006 and 2009 explosion events at Bezymianny volcano with use of a regional atmospheric modeling system. J Volcanol Geotherm Res 270:53–75. https://doi.org/10.1134/S0742046315010054

Moxnes ED, Kristiansen NI, Stohl A, Clarisse L, Durant A, Weber K, Vogel A (2014) Separation of ash and sulfur dioxide during the 2011 Grímsvötn eruption. J Geophys Res Atmos 119:7477–7501. https://doi.org/10.1002/2013JD021129

Pfeiffer T, Costa A, Macedonio G (2005) A model for the numerical simulation of tephra fall deposits. J Volcanol Geotherm Res 140:237–294. https://doi.org/10.1016/j.jvolgeores.2004.09.001

Pielke RA, Cotton WR, Tremback CJ, Nicholls ME, Moran MD, Wesley DA, Lee TJ, Copeland JH (1992) A comprehensive meteorological modeling system—RAMS. Meteorog Atmos Phys 49:69–91. https://doi.org/10.1007/BF01025401

Proussevitch AA, Sahagian DL (2012) The relation between pre-eruptive bubble size distribution and observed ash particle sizes. EGU General Assembly 2012, held 22-27 April, 2012 in Vienna, Austria, p.5953

Pyle DM (1989) The thickness, volume and grainsize of tephra fall deposits. Bull Volcanol 51:1–15. https://doi.org/10.1007/BF01086757

Riley CM, Rose WI, Bluth GJS (2003) Quantitative shape measurements of distal volcanic ash. J Geophys Res 108(B10):2504. https://doi.org/10.1029/2001JB000818

Rose WI, Durant AJ (2009) Fine ash content of explosive eruptions. J Volcanol Geotherm Res 186:32–39. https://doi.org/10.1016/j.jvolgeores.2009.01.010

Rosenblatt M (1956) Remarks on some nonparametric estimates of a density function. Ann Math Stat 27:642–669. https://doi.org/10.1214/aoms/1177728190

Schumacher R (1994) A reappraisal of Mount St. Helens' ash clusters—depositional model from experimental observation. J Volcanol Geotherm Res 59:253–260. https://doi.org/10.1016/0377-0273(94)90099-X

Schumacher R, Schmincke HU (1995) Models for the origin of accretionary lapilli. Bull Volcanol 56:626–639. https://doi.org/10.1007/BF00301467

Spanu A, Michieli Vitturi MD, Barsotti S (2016) Reconstructing eruptive source parameters from tephra deposit: a numerical study of medium-sized explosive eruptions at Etna volcano. Bull Volcanol 78:1–19. https://doi.org/10.1007/s00445-016-1051-2

Sparks RSJ, Bursik MI, Carey SN, Gilbert JS, Glaze LS, Sigurdsson H, Woods AW (1997) Volcanic plumes. John Wiley and Sons Ltd

Spieler O, Alidibirov M, Dingwell DB (2003) Grain-size characteristics of experimental pyroclasts of 1980 Mount St. Helens cryptodome dacite: effects of pressure drop and temperature. Bull Volcanol 65: 90–104. https://doi.org/10.1007/s00445-002-0244-z

Steinke I, Mohler O, Kiselev A, Niemand M, Saathoff H, Schnaiter M et al (2011) Ice nucleation properties of fine ash particles from the Eyjafjallajökull eruption in April 2010. Atmos Chem Phys 11: 12945–12958. https://doi.org/10.5194/acp-11-12945-2011

Stohl A, Prata AJ, Eckhardt S, Clarisse L, Durant A, Henne S, Kristiansen NI, Minikin A, Schumann U, Seibert P, Stebel K, Thomas HE, Thorsteinsson T, Tørseth K, Weinzierl B (2011) Determination of time- and height-resolved volcanic ash emissions for quantitative ash dispersion modeling: the 2010 Eyjafjallajokull eruption. Atmos Chem Phys 11:4333–4351. https://doi.org/10.5194/acp-11-4333-2011

Stuefer M, Freitas SR, Grell G, Webley P, Peckham S, McKeen SA, Egan SD (2013) Inclusion of ash and SO2 emissions from volcanic eruptions in WRF-CHEM: development and some applications. Geosci Model Dev 5:2571–2597. https://doi.org/10.5194/gmd-6-457-2013

Suzuki T (1983) A theoretical model for dispersion of tephra. In: Shimozuru D, Yokoyama I (eds) Arc volcanism, physics and tectonics. Terra, Tokyo, pp 95–113

Taylor GI (1921) Diffusion by continuous movements. Proc Lond Math Soc s2–20:196–212. https://doi.org/10.1112/plms/s2-20.1.196

Textor C, Graf HF, Herzog M, Oberhuber JM, Rose WI, Ernst GGJ (2006) Volcanic particle aggregation in explosive eruption columns. Part I: parameterization of the microphysics of hydrometeors and ash. J Volcanol Geotherm Res 150:359–377. https://doi.org/10.1016/j.jvolgeores.2005.09.007

Tremback CJ, Lyons WA, Thorson WP, Walko RL (1994) An emergency response and local weather forecasting software system. Preprints, Eighth Joint Conf. on the Applications of Air Pollution Meteorology. Amer. Meteor. Soc., Nashville, TN, pp. 219–223

Turner R, Moore S, Pardo N, Kereszturi G, Uddstrom M, Hurst T, Cronin S (2014) The use of numerical weather prediction and a Lagrangian transport (NAME-III) and dispersion (ASHFALL) models to explain patterns of observed ash deposition and dispersion following the August 2012 Te Maari, New Zealand eruption. J Volcanol Geotherm Res 286:437–451 https://doi.org/10.1016/j.jvolgeores.2014.05.017

Varah JM (1973) On the numerical solution of ill-conditioned linear systems with application to ill-posed problems. SIAM J Numer Anal 10:257–267. https://doi.org/10.1137/0710025

Wahba G (1990) Spline models for observational data, CBMS-NSF Regional Conference Series in Applied Mathematics, vol 59. Society for Industrial and Applied Mathematics, Philadelphia, PA

Walker GPL (1971) Grain-size characteristics of pyroclastic deposits. J Geol 79:696–714 https://doi.org/10.1086/627699

Walker GPL (1981) Generation and dispersal of fine ash and dust by volcanic eruptions. J Volcanol Geotherm Res 11:81–92. https://doi.org/10.1016/0377-0273(81)90077-9

Walko RL, Tremback CJ (1995) HYPACT; the hybrid particle and concentration transport model. User's guide. Mission Research Corporation, Ft Collins, CO

Wang L-P, Stock DE (1993) Dispersion of heavy particles in turbulent motion. J Atmos Sci 50:1897–1913. https://doi.org/10.1175/1520-0469(1993)050<1897:DOHPBT>2.0.CO

White JT, Connor CB, Connor L, Hasenaka T (2017) Efficient inversion and uncertainty quantification of a tephra fallout model. J Geophys Res Solid Earth 122:281–294. https://doi.org/10.1002/2016JB013682

Wilson L, Huang T (1979) The influence of shape on the atmospheric settling velocity of volcanic ash particles. Earth Planet Sci Lett 44: 311–324. https://doi.org/10.1016/0012-821X(79)90179-1

Wilson JD, Sawford BL (1996) Review of Lagrangian stochastic models for trajectories in the turbulent atmosphere. Bound-Layer Meteorol 78:191–210. https://doi.org/10.1007/BF00122492

Wohletz KH, Sheridan MF, Brown WK (1989) Particle size distributions and the sequential fragmentation/transport theory applied to volcanic ash. J Geophys Res 94(B11):15703–15721. https://doi.org/10.1029/JB094iB11p15703

Woodhouse MJ, Hogg AJ, Phillips JC, Sparks RSJ (2013) Interaction between volcanic plumes and wind during the 2010 Eyjafjallajökull eruption, Iceland. J Geophys Res 118(B):92–109. https://doi.org/10.1029/2012JB009592

Yamada T, Bunker S (1988) Development of a nested grid, second moment turbulence closure model and application to the 1982 ASCOT Brush Creek data simulation. J Appl Meteorol 27:562–578. https://doi.org/10.1175/1520-0450(1988)027<0562:DOANGS>2.0.CO;2